

# Intermediate-Mass Black Hole Growth and Feedback in Dwarf Galaxies at High Redshifts

Paramita Barai<sup>1</sup>, Elisabete M. de Gouveia Dal Pino<sup>1</sup>

<sup>1</sup> *Instituto de Astronomia, Geofísica e Ciências Atmosféricas - Universidade de São Paulo (IAG-USP), Rua do Matão 1226, São Paulo, 05508-090, Brasil*

18 January 2022

## ABSTRACT

Intermediate-mass black holes (IMBHs: masses between  $100 - 10^6 M_\odot$ ) historically comprise of an elusive population compared to stellar-mass and supermassive BHs. Recently IMBHs have started to be observed at the centers of low-mass galaxies. We perform cosmological hydrodynamical simulations of  $(2h^{-1} \text{ Mpc})^3$  comoving boxes and investigate the growth and feedback of central IMBHs in dwarf galaxies (DGs). The earliest BHs appear at  $z \sim 18 - 25$ , and grow thereafter by accreting gas and by merger with other BHs. We find that, starting from  $10^2 M_\odot$ , it is possible to build up IMBHs of a few  $\times 10^5 - 10^6 M_\odot$  by  $z = 5$ , when the BHs are seeded in halos less massive than  $4 \times 10^7 M_\odot$ . The BH accretion rates increase with time, and reaches  $\dot{M}_{\text{BH}} = (0.2 - 0.8) \dot{M}_{\text{Edd}}$  for the massive IMBHs by  $z = 4$ . The star formation rate density (SFRD) evolution of the DGs (stellar mass  $10^5 - 10^8 M_\odot$ ) has a peak plateau between  $z = 4 - 6$ . Star formation is quenched between  $z = 9 - 4$ . The SFRD is reduced by factors up to 3, when the BHs have grown to a few times  $10^5 M_\odot$ . Even in the presence of stronger SN-driven mass ejection, the BHs continue to grow up to  $z \sim 6$ , sustained by gas inflows driven by galaxy mergers and interactions in a cosmological environment. Our conclusions, based on numerical simulation results, support the scenario that early feedback from IMBHs in gas-rich DGs at  $z = 5 - 8$  can potentially solve several anomalies in the DG mass range within the concordance  $\Lambda$ CDM cosmological scenario (Silk 2017). Our results suggest that IMBHs at DG centers grow faster than their host galaxies in the early Universe, and the resulting BH feedback turns the DGs and the BHs dormant.

**Key words:** (cosmology:) large-scale structure of Universe – galaxies: dwarf – galaxies: high-redshift – (galaxies:) quasars: supermassive black holes – black hole physics – hydrodynamics

## 1 INTRODUCTION

Black holes (BHs) are usually observed to be of stellar-mass ( $M_{\text{BH}} \sim 1 - 100 M_\odot$ ), or supermassive ( $M_{\text{BH}} \sim 10^6 - 10^9 M_\odot$ ). Stellar-mass BHs have been historically observed in X-ray binaries existing in our Milky Way and other galaxies (e.g., Bolton 1972; Cowley et al. 1983; Orosz et al. 2007; Corral-Santana et al. 2016), and more recently in globular clusters (e.g., Maccarone et al. 2007; Giesers et al. 2018). Supermassive BHs (SMBHs) are believed to exist at the centers of active galactic nuclei (AGN), which liberate enormous amounts of feedback energy powered by the accretion of matter (e.g., Rees 1984; Ferrarese & Ford 2005). AGN are widely observed through their multi-wavelength emission at all cosmic epochs,  $z = 0 - 7$ , starting from the lo-

cal Universe up to 13 Gyr ago (e.g., Urry & Padovani 1995; Goulding & Alexander 2009; Mortlock et al. 2011).

Intermediate-mass black holes (IMBHs) of masses between  $100 - 10^6 M_\odot$  (e.g., van der Marel 2004; Graham et al. 2018) are however not as widely observed. Some studies argue that the accreting BHs in ultra-luminous X-ray sources could be IMBHs (e.g., Miller et al. 2003; Sutton et al. 2012; Caballero-Garcia et al. 2018; Mezcua et al. 2018b), based on the calculation of the BH mass from a cold thermal disc accreting at sub-Eddington rates.

We do not know how the SMBHs in AGN grew to billions of solar masses. In one scenario, the SMBHs could grow from stellar-mass BHs by rapid enhanced accretion (e.g. super-Eddington growth). Or, some exotic processes in the early Universe could have formed massive BH seeds (in the

direct collapse scenario) soon after the Big Bang. Massive seed IMBHs could be a possible explanation for the origin of SMBHs. A recent study by Kovetz et al. (2018) suggest that gravitational wave measurements using the advanced LIGO over six years can be used to limit the formation mechanism of IMBHs by the runaway merger of stellar-mass BHs in globular clusters.

Relatively recently, massive BHs have started to be observed hosted in Dwarf Galaxies (DGs). Dynamical BH mass limits detected in nearby dwarfs include several examples such as:  $M_{\text{BH}} \sim 3 \times 10^6 M_{\odot}$  in the dwarf elliptical galaxy M32 (van der Marel et al. 1998);  $M_{\text{BH}} \sim 10^5 M_{\odot}$  in the dwarf lenticular field galaxy NGC 404 (Seth et al. 2010);  $M_{\text{BH}} < 2 \times 10^4 M_{\odot}$  in the dwarf elliptical galaxy NGC 205 (Valluri et al. 2005); and  $M_{\text{BH}} < 10^6 M_{\odot}$  in the dwarf spheroidal galaxy Ursa Minor (Demers et al. 1995).

Some of the central IMBHs in DGs show signatures of activity in the form of low-luminosity AGN. NGC 4395 is a bulgeless dwarf galaxy with an extremely faint Seyfert 1 nucleus (Filippenko & Sargent 1989), and an estimated central BH mass  $M_{\text{BH}} \sim 10^4 - 3 \times 10^5 M_{\odot}$  (Peterson et al. 2005; Woo et al. 2019). Pox 52 (G 1200-2038) is a dwarf galaxy with Seyfert characteristics (Kunth, Sargent & Bothun 1987), having a central BH of  $M_{\text{BH}} \sim (2 - 4) \times 10^5 M_{\odot}$  (Thornton et al. 2008). The dwarf starburst galaxy Henize 2-10 (Reines et al. 2011) has an actively accreting massive BH with an order-of-magnitude mass  $M_{\text{BH}} \sim 10^6 M_{\odot}$ .

The population of DGs with observed AGN signatures have been increasing (e.g., Chilingarian et al. 2018). Izotov & Thuan (2008) presented the spectra of 4 low-metallicity DGs with very-high broad H $\alpha$  luminosities, most likely coming from accretion disks around IMBHs ( $5 \times 10^5 \leq M_{\text{BH}} \leq 3 \times 10^6 M_{\odot}$ ). Performing a systematic search for AGN in DGs using optical spectroscopy from the SDSS, Reines, Greene & Geha (2013) found 136 DGs, with stellar mass between  $10^{8.5} < M_{\star} < 10^{9.5} M_{\odot}$  at  $z < 0.055$ , hosting active massive BHs with virial BH masses in the range  $10^5 < M_{\text{BH}} < 10^6 M_{\odot}$ . Using SDSS DR7, Moran et al. (2014) identified 28 nearby low-mass, low-luminosity DGs containing accreting IMBHs ( $10^3 \leq M_{\text{BH}} \leq 10^6 M_{\odot}$ ) at their centers, and derived a lower limit of a few percent on the fraction of DGs containing AGN.

The BH mass versus stellar mass relationship of IMBHs in DGs tend to be below the existing local relation extending into the lower galaxy mass regime (e.g., Baldassare et al. 2015; Reines & Volonteri 2015). Albeit there is a large scatter, and exceptions i.e. IMBHs lying on the  $[M_{\text{BH}} - \sigma_{\star}]$  local relation when extended to lower masses (e.g., Woo et al. 2019). IMBH candidates detected using deep X-ray observations (e.g., Schramm et al. 2013; Secret et al. 2015; Lemons et al. 2015) show that low-mass galaxies with  $M_{\star} < 3 \times 10^9 M_{\odot}$  have BHs of  $M_{\text{BH}} \sim 2 \times 10^5 M_{\odot}$ . The most-massive ultracompact dwarf galaxy M59-UCD3 with  $M_{\star} \sim 2 \times 10^8 M_{\odot}$  has a massive central BH of  $M_{\text{BH}} \sim 4 \times 10^6 M_{\odot}$  (Ahn et al. 2018). The Fornax UCD3 hosting a central  $M_{\text{BH}} \sim 3.3 \times 10^6 M_{\odot}$  corresponds to 4% of the galaxy stellar mass (Afanasiev et al. 2018). Marleau et al. (2017) investigated the presence of AGN in nearby galaxies using mid-infrared emission, and found some DGs in their sample. These DGs have stellar masses between  $10^6 - 10^9 M_{\odot}$ , and the BH masses (estimated from their IR luminosity, as-

suming a bolometric luminosity of 10% of the Eddington) in the range  $10^3 - 10^6 M_{\odot}$ .

Recently the highest-redshift discovery of AGN in DGs has been made by Mezcua et al. (2018a). They present a sample of 40 AGN of type 2 at  $z \leq 2.4$  with luminosities in the range  $L_{0.5-10\text{keV}} \sim 10^{39} - 10^{44}$  erg/s. The hosts are DGs with stellar masses between  $10^7 - 3 \times 10^9 M_{\odot}$ , selected from the Chandra COSMOS-Legacy survey. Estimating the BH masses using the local scaling relation between BH and stellar mass (Reines & Volonteri 2015), all the AGN are consistent with hosting  $\sim 10^4 - 10^5 M_{\odot}$  IMBHs (with a scatter of 0.55 dex), of typical Eddington ratios (or, the ratio of the BH accretion rate to the Eddington rate)  $> 1\%$ . According to Mezcua et al. (2018a), the observational trends suggest that AGN in DGs evolve differently than those in more-massive galaxies.

AGN influence the formation and evolution of galaxies in the form of feedback, affecting the environment from pc to Mpc scales (e.g., Silk & Rees 1998; Barai 2008; Fabian 2012). Supermassive BHs and host galaxies are argued to coevolve, generating observational trends such as the central BH mass - host galaxy stellar bulge mass correlations (e.g., Magorrian et al. 1998; Gebhardt et al. 2000). The SMBH energy output is often observed as various forms of AGN outflows (e.g., Crenshaw, Kraemer & George 2003; Cicone et al. 2014; Melioli & de Gouveia Dal Pino 2015; Tombesi et al. 2015; Barai et al. 2018).

Analogous to SMBHs producing AGN feedback, the IMBHs are also expected to have feedback: the energy radiated by IMBHs should affect their host galaxies, possibly driving galactic outflows. BH or AGN feedback mechanism has recently started to be observed in low-mass galaxies. Penny et al. (2017) presented observational evidence for AGN feedback in a sample of 69 quenched low-mass galaxies ( $M_{\star} < 4 \times 10^9 M_{\odot}$ ); including 6 galaxies showing signatures of an active AGN preventing ongoing star-formation. At the same time, supernova feedback should also be operating parallelly in these low-mass galaxies, ejecting out gas (e.g., Caproni et al. 2017).

AGN feedback operates mostly in the negative form quenching star formation, as indicated by simulations (e.g., Scannapieco, Silk & Bouwens 2005; Barai et al. 2014), and some observations (e.g., Schawinski et al. 2006; Lanz et al. 2016). At the same time, AGN outflows can occasionally compress clumpy gas clouds and trigger starbursts, bringing in positive AGN feedback, as found in numerical studies (e.g., De Young 1989; Bieri et al. 2015; Mukherjee et al. 2018), and observed in jet-induced star formation (e.g., Chambers, Miley & van Breugel 1987; Viegas & de Gouveia dal Pino 1992; Zinn et al. 2013; Salome et al. 2017). In this work we focus on negative BH feedback effects where star-formation is quenched.

The concordance  $\Lambda$ CDM cosmological scenario of galaxy formation presents multiple anomalies in the dwarf galaxy mass range: e.g. core-cusp, number of DGs. Recently Silk (2017) made an exciting theoretical claim that the presence of IMBHs at the centers of essentially all old DGs can potentially solve the problems. Early feedback energy from these IMBHs can affect the host gas-rich dwarf galaxies at  $z = 5 - 8$ . This early feedback can quench star-formation, reduce the number of DGs, and impact the density profile at DG centers. Dashyan et al. (2018) studied the same prob-

lem analytically using a constant luminosity of the AGN, and compared AGN versus supernova (SN) feedback. They find a critical halo mass below which the central AGN can drive gas out of the host halo. This negative feedback effect of AGN is found to be more efficient than SN in the most-massive DGs, where SN is not able to expel the gas. Noteworthy that some numerical simulations find that AGN feedback is inefficient in low-mass galaxies (Dubois et al. 2015; Habouzit et al. 2017; Angles-Alcazar et al. 2017; Prieto et al. 2017; Trebitsch et al. 2018), because strong SN feedback hampers BH growth by removing gas from around the BH. Such a scenario is also supported by observational studies (Martin-Navarro & Mezcua 2018) indicating that AGN activity does not dominate baryonic cooling in low-mass galaxies where SN feedback prevails.

In this work, we investigate the scenario that IMBHs are present at the centers of dwarf galaxies, by performing cosmological hydrodynamical simulations. Our goals are to (i) test if IMBHs would grow at DG centers in a cosmological environment, and (ii) quantify the impact of feedback from IMBHs on their host DGs, especially the effects on star formation at cosmic epochs  $z = 6 - 4$ .

This paper is organised as follows: our numerical code and simulation setup are described in §2, our results are presented and analyzed in §3, and a summary of our main findings are given in §4.

## 2 NUMERICAL METHOD

We use a modified version of the code GADGET-3 (Springel 2005), which uses the TreePM (particle mesh) and SPH (smoothed particle hydrodynamics) methods. It includes sub-resolution physics as described in §2.1 and §2.2. The physics of multiphase structure of the interstellar medium (ISM), on scales unresolved in cosmological simulations, is modeled using spatially averaged properties describing the medium on scales that are resolved. Our different simulation runs are outlined in §2.3.

### 2.1 Cooling, Star-Formation, SN Feedback

Radiative cooling and heating is implemented, including metal-line cooling (Wiersma, Schaye & Smith 2009). In this model, net cooling rates are computed element-by-element tracking 11 atomic species: H, He, C, Ca, O, N, Ne, Mg, S, Si, Fe. A spatially-uniform time-dependent photoionizing background radiation is considered from the cosmic microwave background and the Haardt & Madau (2001) model for the ultraviolet/X-ray background. The gas is assumed to be dust free, optically thin, and in (photo-) ionization equilibrium. Contributions from the 11 elements are interpolated as a function of density, temperature and redshift from tables that have been pre-computed using the public photoionization code CLOUDY (last described by Ferland et al. 1998).

Star formation (SF) is adopted following the multiphase effective sub-resolution model of Springel & Hernquist (2003). Gas particles with density above a limiting threshold,  $\rho_{\text{SF}} = 0.13 \text{ cm}^{-3}$  (in units of number density of hydrogen atoms), represent cold and hot phase regions of the ISM. The unresolved cold condensed clouds (comprising of fraction  $x$  of a gas particle) are in pressure equilibrium with the

ambient hot gas. The star formation rate of the high-density gas particle (of mass  $m_{\text{gas}}$ ) is estimated using a Schmidt-type law (Schmidt 1959):  $\dot{m}_* = xm_{\text{gas}}/t_*$ . Here,  $xm_{\text{gas}}$  is the mass of cold clouds supplying the material available for SF. The SF time-scale ( $t_*$ ) of the gas particle is computed as a function of gas density:  $t_*(\rho) = t_0^*(\rho/\rho_{\text{SF}})^{-1/2}$ , where  $t_0^*$  is a parameter of the model. We use a value of  $t_0^* = 1.5 \text{ Gyr}$  (Springel & Hernquist 2003; Tornatore et al. 2007), chosen to reproduce the observed relation between the disc-averaged SF per unit area and the gas surface density (Kennicutt 1998). The star forming gas remains in self-regulated equilibrium. Star particles are collisionless, and are spawned from these high-density gas particles, according to a stochastic scheme (Katz, Weinberg & Hernquist 1996).

Stellar evolution and chemical enrichment are computed for the 11 elements (Tornatore et al. 2007). Each star particle is treated as a simple stellar population (SSP). Given a stellar initial mass function (IMF), the mass of the SSP is varied in time following the death of stars, and accounting for stellar mass losses. A fixed stellar initial mass function (Chabrier 2003) is included, in the mass range  $(0.1 - 100)M_\odot$ . Stars within a mass interval  $[8 - 40]M_\odot$  become SN first before turning into stellar-mass black holes at the end of their lives, while stars of mass  $> 40M_\odot$  are allowed to directly end in black holes without contributing to gas enrichment.

Feedback from supernovae is incorporated in the kinetic form, assuming a mass ejection rate  $\dot{M}_{\text{SN}}$  proportional to the star formation rate ( $\dot{M}_*$ ):

$$\dot{M}_{\text{SN}} = \eta \dot{M}_*. \quad (1)$$

The mass loading factor of SN wind is taken as  $\eta = 2$  (e.g., Tornatore et al. 2007; Barai et al. 2013; Melioli, de Gouveia Dal Pino & Geraissate 2013), following observations revealing that SN-driven outflow rates are comparable to or larger than SF rates of galaxies (e.g., Martin 1999; Bouche et al. 2012). The SN wind kinetic power is a fixed fraction  $\chi$  of SN internal energy rate:

$$\frac{1}{2} \dot{M}_{\text{SN}} v_{\text{SN}}^2 = \chi \epsilon_{\text{SN}} \dot{M}_*. \quad (2)$$

Here  $v_{\text{SN}}$  is the SN wind velocity,  $\epsilon_{\text{SN}}$  is the average energy released by SN for each  $M_\odot$  of stars formed under the instantaneous recycling approximation. For our adopted Chabrier (2003) power-law IMF,  $\epsilon_{\text{SN}} = 1.1 \times 10^{49} \text{ erg } M_\odot^{-1}$ . Combining above expressions,  $v_{\text{SN}}$  can be re-written as:  $v_{\text{SN}} = (2\chi\epsilon_{\text{SN}}/\eta)^{1/2}$ . Following a series of studies (e.g., Tornatore et al. 2007; Tescari et al. 2011; Barai et al. 2013), and unlike (Springel & Hernquist 2003), we choose  $v_{\text{SN}}$  as a free parameter. We adopt a constant-velocity outflow with SN wind velocity  $v_{\text{SN}} = 350 \text{ km/s}$  (as was done in e.g. Tornatore et al. 2007; Barai et al. 2015; Biffi et al. 2016).

The numerical implementation of launching SN wind in the GADGET-3 code involves a probabilistic criteria similar to spawning star particles (following e.g., Springel & Hernquist 2003; Barai et al. 2013). It assumes there is no time delay between star formation and SN explosions. A probability is calculated in a timestep  $\Delta t$  for each high-density multiphase gas particle:

$$p = 1 - \exp\left(-\frac{\eta x \Delta t}{t_*}\right). \quad (3)$$

A random number is drawn in the interval  $[0, 1]$ , and if it

is below  $p$  then the gas particle is given a SN wind kick. If  $\vec{v}$  is particle velocity and  $\phi$  its gravitational potential, then its velocity is updated to:  $\vec{v}_{\text{new}} = \vec{v}_{\text{old}} + v_{\text{SN}}\hat{y}$ . The direction (unit vector  $\hat{y}$ ) is set along positive or negative ( $\vec{v}_{\text{old}} \times \vec{\nabla}\phi$ ), which makes the SN wind particles to be preferentially ejected along the rotation axis of the galaxy or perpendicular to the galaxy disk.

In order to enable the SN outflows to escape from dense SF regions without affecting the SF, the new SN wind particle is decoupled from hydrodynamic interactions, for a maximum duration  $t_{\text{dec}} = 0.025t_{\text{H}}(z)$ , where  $t_{\text{H}}(z)$  is the Hubble time at a relevant simulation redshift. Then the SN wind particle does not enter in the hydrodynamic force computation in the code, but it is included in the gravity and SPH density calculations. If the gas particle's density has fallen below  $\rho_{\text{dec}} = 0.25\rho_{\text{SF}}$ , then the decoupling is stopped before  $t_{\text{dec}}$ , and full hydrodynamics is enabled again.

## 2.2 BH Accretion and Feedback

BHs are collisionless sink particles (of mass  $M_{\text{BH}}$ ) in our simulations. A BH (of initial mass  $M_{\text{BHseed}}$ ) is seeded at the center of each halo more massive than a total mass  $M_{\text{HaloMin}}$ , which does not contain a BH yet. Halos are identified by executing a *Friends-of-Friends* (FOF) group finder on-the-fly within our simulations. We test different values of minimum halo mass and seed BH mass in the range:  $M_{\text{HaloMin}} = (10^6 - 5 \times 10^7)M_{\odot}$ , and  $M_{\text{BHseed}} = (10^2 - 10^4)M_{\odot}$ .

Gas is considered to accrete onto a BH according to the Bondi-Hoyle-Lyttleton accretion rate ( $\dot{M}_{\text{Bondi}}$ : Hoyle & Lyttleton 1939; Bondi 1952),

$$\dot{M}_{\text{Bondi}} = \alpha \frac{4\pi G^2 M_{\text{BH}}^2 \rho}{(c_s^2 + v^2)^{3/2}}, \quad (4)$$

where  $G$  is the gravitational constant,  $c_s$  is the sound speed,  $\rho$  is the gas density,  $v$  is the velocity of the BH relative to the gas, and  $\alpha = 100$  is a numerical boost factor (e.g., Springel, Di Matteo & Hernquist 2005; Johansson, Naab & Burkert 2009; Dubois et al. 2013). Furthermore, accretion is limited to the Eddington mass accretion rate ( $\dot{M}_{\text{Edd}}$ ):  $\dot{M}_{\text{BH}} = \min(\dot{M}_{\text{Bondi}}, \dot{M}_{\text{Edd}})$ . The Eddington luminosity is used to express the Eddington mass accretion rate,

$$L_{\text{Edd}} = \frac{4\pi G M_{\text{BH}} m_p c}{\sigma_T} = \epsilon_r \dot{M}_{\text{Edd}} c^2, \quad (5)$$

where  $m_p$  is the mass of a proton,  $c$  is the speed of light, and  $\sigma_T$  is the Thomson scattering cross-section for an electron.

The implementation in the GADGET-3 code involves computing a BH smoothing length  $h_{\text{BH}}$ . It is determined by the implicit solution of the following equation at each timestep,

$$\frac{4}{3}\pi h_{\text{BH}}^3 \rho_{\text{BH}} = M_{\text{ngb}}, \quad (6)$$

where  $\rho_{\text{BH}}$  is the density at the position of the BH, and  $M_{\text{ngb}}$  is the mass of 200 neighboring gas particles. A maximum of  $100L_{\text{soft}}$  (with  $L_{\text{soft}} =$  gravitational softening length, viz. §2.1 of Springel (2005)) is set for the possible value of  $h_{\text{BH}}$ . A sphere of radius  $h_{\text{BH}}$  is used to compute accretion onto the BH of neighboring gas particles, using a stochastic methodology at every timestep (for details see §2.1 and

§2.3 of Barai et al. 2014). Physical quantities (e.g.  $\rho$ ,  $c_s$ ,  $v$  in Eq. (4)) are computed dynamically within the code, using the SPH kernel-weighted smoothing method over gas particles neighboring every BH particle.

Feedback energy is distributed to the surrounding gas, according to:

$$\dot{E}_{\text{feed}} = \epsilon_f \epsilon_r \dot{M}_{\text{BH}} c^2. \quad (7)$$

Here  $\epsilon_r$  is the radiative efficiency, and  $\epsilon_f$  is the feedback efficiency. We adopt  $\epsilon_r = 0.1$ , which assumes radiatively efficient accretion onto a Schwarzschild BH (Shakura & Sunyaev 1973).

Kinetic BH feedback is included (Barai et al. 2014, 2016), where the neighboring gas is pushed outward with a velocity  $v_w$  and mass outflow rate  $\dot{M}_w$ . Using the conservation of energy,  $\frac{1}{2}\dot{M}_w v_w^2 = \dot{E}_{\text{feed}}$ , and Eq. (7), the BH kinetic outflow rate can be written as,

$$\dot{M}_w = 2\epsilon_f \epsilon_r \dot{M}_{\text{BH}} \frac{c^2}{v_w^2}. \quad (8)$$

We use the values:  $\epsilon_f = 0.05$ , and the range  $v_w = 1000, 2000, 5000, 10000$  km/s.<sup>1</sup>

The BH kinetic feedback energy is distributed to the gas within a distance  $h_{\text{BH}}$  from the BH. A bi-cone volume is defined around the BH, of slant height  $h_{\text{BH}}$  and half-opening angle  $45^\circ$ . The cone-axis direction is randomly assigned during a BH seeding, and remains fixed henceforth for each BH. The total gas mass within the bi-cone  $M_{\text{gas}}^{\text{vicinity}}$  is computed. A probability is calculated for the  $i$ 'th gas particle inside the bi-cone, in a timestep  $\Delta t$ :

$$p_i = \frac{\dot{M}_w \Delta t}{M_{\text{gas}}^{\text{vicinity}}}, \quad (9)$$

where  $\dot{M}_w$  is the mass outflow rate obtained from Eq. (8). A random number  $x_i$  is drawn uniformly distributed in the interval  $[0, 1]$ . If  $x_i < p_i$ , then the gas particle is imparted a velocity boost by AGN wind, such that:

$$\vec{v}_{\text{new}} = \vec{v}_{\text{old}} + v_w \hat{n}. \quad (10)$$

The AGN wind direction  $\hat{n}$  is considered radially outward from the BH.

We incorporate a scheme for BH *pinning*<sup>2</sup>, or *BH advection algorithm* (also done in e.g., Springel, Di Matteo & Hernquist 2005; Wurster & Thacker 2013; Schaye et al. 2015). Each BH is repositioned at each

<sup>1</sup> We notice that, although most of the adopted values of the AGN wind velocity in our models are smaller than those inferred from observations of AGN ultra-fast outflows (e.g., Melioli & de Gouveia Dal Pino 2015; Kraemer, Tombesi & Bottorff 2018, and references therein), the few tests we performed with more compatible values around 10000 km/s did not reveal significant differences in the results (for more details see §3).

<sup>2</sup> The BH seeds start as  $10^2 M_{\odot}$  and  $10^3 M_{\odot}$  in most of our simulations (Table 1), which is of the order of 1/100th of the gas and DM particle's mass (§2.3). Such low-mass BHs are susceptible to dynamical movements and wander away from galaxy centres (as seen in e.g., Barai et al. 2018), by interactions with neighboring more-massive gas and DM particles. Therefore a reposition algorithm is often adopted in SPH simulations to keep the BH at the galaxy center.

**Table 1.** Simulation runs and parameters.

Run name	SN Wind Feedback Mass Load Factor, $\eta$	BH present	Min. Halo Mass for BH Seeding, $M_{\text{HaloMin}}[M_{\odot}]$	Seed BH Mass, $M_{\text{BHseed}}[M_{\odot}]$	BH kinetic feedback kick velocity $v_w$ (km/s)
<i>noSN-noBH</i>	–	No	–	–	–
<i>SN</i>	2	No	–	–	–
<i>BHs2h1e6v2</i>	2	Yes	$1 \times 10^6$	$10^2$	2000
<i>BHs2h1e6v10</i>	2	Yes	$1 \times 10^6$	$10^2$	10000
<i>BHs2h4e7v2</i>	2	Yes	$4 \times 10^7$	$10^2$	2000
<i>BHs2h7e7v2</i>	2	Yes	$7 \times 10^7$	$10^2$	2000
<i>BHs3h1e7v2</i>	2	Yes	$1 \times 10^7$	$10^3$	2000
<i>BHs3h1e7v2-SNhi</i>	5	Yes	$1 \times 10^7$	$10^3$	2000
<i>BHs3h2e7v2</i>	2	Yes	$2 \times 10^7$	$10^3$	2000
<i>BHs3h3e7v2</i>	2	Yes	$3 \times 10^7$	$10^3$	2000
<i>BHs3h3e7v1</i>	2	Yes	$3 \times 10^7$	$10^3$	1000
<i>BHs3h4e7v1</i>	2	Yes	$4 \times 10^7$	$10^3$	1000
<i>BHs3h4e7v2</i>	2	Yes	$4 \times 10^7$	$10^3$	2000
<i>BHs3h4e7v5</i>	2	Yes	$4 \times 10^7$	$10^3$	5000
<i>BHs3h4e7v10</i>	2	Yes	$4 \times 10^7$	$10^3$	10000
<i>BHs3h5e7v2</i>	2	Yes	$5 \times 10^7$	$10^3$	2000
<i>BHs4h4e7v2</i>	2	Yes	$4 \times 10^7$	$10^4$	2000

time-step to the location of the minimum gravitational potential of its host galaxy (Barai et al. 2018). However such an algorithm has the limitation that it might overestimate the accretion rate onto the BH, because of forcing it to be positioned near the highest gas density location at the galaxy center. Note that we do not consider any dynamical friction effects experienced by a BH as it orbits within its host galaxy, which is expected to become important at sub-kpc and smaller scales according to higher resolution simulations (e.g., Tremmel et al. 2015). Such scales are generally lower than or of the order of the BH smoothing length ( $h_{\text{BH}}$ ) in our simulations, and thus not resolved. Therefore the BH dynamics is effectively replaced by the numerical advection algorithm.

We consider that when galaxies merge during hierarchical structure assembly, their hosted central BHs merge as well. In the numerical algorithm, two BH particles are allowed to merge to form a single BH, when the distance between them is smaller than the smoothing length of either one and their relative velocity is below the local sound speed (e.g., Sijacki et al. 2007; Di Matteo et al. 2012). The final merged BH has a mass equal to the sum of the BH masses, and a velocity along the center of mass of the initial two merging BHs. To impart kinetic feedback energy, the merged BH retains the bi-cone axis direction of the more massive initial BH.

### 2.3 Simulations

We perform cosmological hydrodynamical simulations of small-sized boxes to probe dwarf galaxies at high redshifts. The initial condition at  $z = 100$  is generated using the MUSIC<sup>3</sup> software (Hahn & Abel 2011). The concordance flat  $\Lambda$ CDM cosmological model is used:  $\Omega_{M,0} = 0.3089$ ,  $\Omega_{\Lambda,0} = 0.6911$ ,  $\Omega_{B,0} = 0.0486$ ,  $H_0 = 67.74 \text{ km s}^{-1} \text{ Mpc}^{-1}$  (Planck Collaboration 2015, results XIII).

<sup>3</sup> MUSIC - Multi-scale Initial Conditions for Cosmological Simulations: <https://bitbucket.org/ohahn/music>

The size of the cubic cosmological volume is  $(2h^{-1} \text{ Mpc})^3$  comoving. Note that we adopt this volume in order to allow for the formation of a larger number of less massive (dwarf) galaxy systems than in typical larger box simulations. We used a single random realization of this box volume, and varied the sub-resolution physical parameters in the different simulations as described next. We use  $256^3$  dark matter and  $256^3$  gas particles in the initial condition. The dark matter particle mass is  $m_{\text{DM}} = 3.44 \times 10^4 h^{-1} M_{\odot}$ , and the gas particle mass is  $m_{\text{gas}} = 6.43 \times 10^3 h^{-1} M_{\odot}$ . The gravitational softening length is set as  $L_{\text{soft}} = 0.1 h^{-1} \text{ kpc}$  comoving. Starting from  $z = 100$ , the box is subsequently evolved up to  $z = 4$ , with periodic boundary conditions.

We execute a series of simulations, with characteristics listed in Table 1. All the runs incorporate metal cooling, chemical enrichment, SF and SN feedback. The first run has no BH, while the remaining runs include BHs. We vary 3 parameters (which were introduced in §2.2) exploring different BH sub-resolution models: the minimum halo mass for BH seeding ( $M_{\text{HaloMin}}$ ), the seed BH mass ( $M_{\text{BHseed}}$ ), and the kick velocity for BH kinetic feedback ( $v_w$ ). These parameters were observed to have the largest effect on the BH growth and feedback. The simulation names are formatted like below, where  $X$ ,  $Y$ ,  $Z$  and  $A$  are numbers in the BH runs.

- *SN* : no BH present. This is a control simulation in which only cooling, enrichment, star-formation, and SN feedback are implemented.

- *BHsXhYeZvA* : with BH accretion and feedback. The parameter values are,  $M_{\text{BHseed}} = 10^X M_{\odot}$ ,  $M_{\text{HaloMin}} = Y \times 10^Z M_{\odot}$ , and  $v_w = A \times 1000 \text{ km/s}$ .

Halos are first identified using the FOF algorithm. A halo is required to contain a minimum of 32 particles. Galaxies are tracked within our simulations using the subhalo finder *SubFind*, which associates substructures to FOF halos. The minimum number of particles to make a valid subhalo is 20. The centre of each galaxy is considered as the location of the gravitational potential minimum of its subhalo. We define galaxy stellar mass as the mass of all star

particles inside the subhalos obtained by the subhalo finder *SubFind*. The halo mass ( $M_{\text{halo}}$ ) of a galaxy, and its virial radius in comoving coordinates ( $R_{200}$ ), are related such that  $R_{200}$  encloses a density 200 times the mean comoving matter density of the Universe:

$$M_{\text{halo}} = \frac{4\pi}{3} R_{200}^3 (200\rho_{\text{crit}}\Omega_{M,0}), \quad (11)$$

where  $\rho_{\text{crit}} = 3H_0^2/(8\pi G)$  is the present critical density.

### 3 RESULTS AND DISCUSSION

#### 3.1 Large Scale Environment

The gas morphology in our simulation box, or the large scale structures, is plotted in Fig. 1. It displays gas properties in the whole  $(2000h^{-1} \text{ kpc})^3$  comoving volume at  $z = 4$ , for two simulations: *SN* (left column), and *BHs3h4e7v2* (right column) - which is a run that produced one of the most-massive BH at  $z = 4$ . The overdensity (i.e., the ratio between the gas density and the cosmological mean baryon density in the Universe), temperature, and star-formation rate (SFR) of the gas are plotted in the three rows from the top. The black circles in the top row depict the virial radius  $R_{200}$  (defined in Eq. 11) of dwarf galaxies with halo masses in the range  $10^8 \leq M_{\text{halo}} \leq 10^9 M_{\odot}$ . The red circles show the  $R_{200}$  of relatively massive galaxies, those having higher halo masses  $M_{\text{halo}} > 10^9 M_{\odot}$ .

The spatial locations of the BHs within our *BHs3h4e7v2* simulation box can be visualized in the top-right panel of Fig. 1, overplotted with the gas overdensity. Here the magenta cross-points designate BH positions, with the symbol size proportional to BH mass. In this run, BHs are seeded at the centres of galaxies with  $M_{\text{HaloMin}} = 4 \times 10^7 M_{\odot}$ . Therefore all the red circles ( $M_{\text{halo}} > 10^9 M_{\odot}$  galaxies) and most of the black circles ( $M_{\text{halo}} = 10^8 - 10^9 M_{\odot}$  galaxies) contain BHs at their centres.

The cosmological large-scale-structure filaments are visible in all the panels of both the runs. There are three Mpc-scale filaments: extending from east to north, from west to north, and from west to south. In addition, there is an overdense region running from the center of the box to the south-west. The filaments consist of dense (yellow and white regions in the top panels), and star-forming (lightgreen, yellow, red and white regions in the bottom panels) gas. The massive galaxies (red circles) lie at the high-density intersections of the filaments, or in the filaments.

In terms of temperature, the immediate vicinity of the dense filaments consists of hotter gas ( $T \sim 10^{4.6}$  K, red regions in the middle panels of Fig. 1), as compared to that in the low-density intergalactic medium and voids (yellow and blue regions). Several mechanisms play together to heat the gas to higher temperatures in the filament vicinity. There are global environmental processes like shock heating during galaxy mergers, and large-scale-structure formation, which are present in both the *SN* and *BHs3h4e7v2* runs. Acting together there are local galactic processes like feedback driven by SN (present in both the columns), and BHs (present in the right column only), which heats the gas, and also often generate outflows.

As they accrete and grow, the BHs provide feedback energy (according to the prescription described in §2.2), which

may drive gas outflows. High-velocity gas ejected by central BH feedback propagates radially outward, and shocks with the surrounding slower-moving gas, creating bubble-like gas outflows. Our simulation *BHs3h4e7v2* shows the formation of BH feedback-induced outflows, as can be seen in Fig. 1 in the top-right half of the right column panels, around the most-massive BH. The outflows are extended bipolar oval-shaped regions along the north-east to south-west direction, propagating to about  $10 \times R_{200}$ . The outflows consist of hot ( $T > 10^{4.6}$  K) - visible as red areas in the temperature map (middle-right panel), and low-density gas (top-right panel).

#### 3.2 Black Hole Accretion and Growth

Fig. 2 presents the BH mass growth with redshift of the most-massive BH for eleven simulations of Table 1. The first BHs are seeded at  $z \sim 18 - 25$  in our simulations, when the first halos reach the corresponding lower limit  $M_{\text{HaloMin}} = (10^6 - 7 \times 10^7) M_{\odot}$ . In some of the runs, one of these first seeds grow to become the most-massive BH. However in runs *BHs3h4e7v2* (maroon solid curve) and *BHs4h4e7v2* (yellow solid curve), the BH which becomes most-massive is seeded at later epochs  $z \sim 7.5 - 12$ . This variance in the seed epochs is because of the different BH growth modes, as described next.

Each BH starts as an initial seed of  $M_{\text{BHseed}} = (10^2, 10^3, 10^4) M_{\odot}$ . The subsequent growth is due to merger with other BHs and gas accretion. When two galaxies containing BHs merge during hierarchical structure formation, their central BHs merge as well (according to the prescription in §2.2) to form a single larger BH. In addition, BHs grow in mass by accreting dense gas from their surroundings, as galaxies evolve and gas inflows to their centres.

We find that in general, when seeded in larger halos, BHs start to grow later and have an overall smaller growth at the same redshift (comparing indigo and magenta curves, for instance). Furthermore, larger seed BHs grow more massive earlier than smaller seeds (comparing yellow and maroon curves), as naively expected. We also find that varying the  $M_{\text{HaloMin}}$  and  $M_{\text{BHseed}}$  together has a competing effect on the BH mass growth, which might cancel each other. A BH can grow similarly when seeded in smaller halos with a smaller seed mass (red curve), as in larger halos with a higher seed mass (indigo curve).

Comparing the blue-dashed (run *BHs3h4e7v1*) versus maroon-solid (run *BHs3h4e7v2*) curves, we find that the final BH masses at  $z = 4$  are comparable. However there is a significant difference in the epoch at which the BHs are seeded, while the only parameter variation between these runs is the BH wind velocity. This occurs because Fig. 2 shows only the most-massive BH, and there are variations in the growth assembly of BHs caused by a coupling between the underlying physics and cosmological hierarchical mergers. In one simulation there can be 2 massive BHs of comparable masses (e.g., seen by the magenta cross-points in Fig. 1 top-right panel), which were seeded at different epochs. So even though the seeding in these runs should be uniform, in *BHs3h4e7v2* a BH which was seeded at a later epoch  $z = 7$  grows to become the largest, whereas in *BHs3h4e7v1* the largest was seeded at  $z = 12$ .

Fig. 3 displays the accretion rate evolution with redshift, of the most-massive BH in each run: BH mass ac-

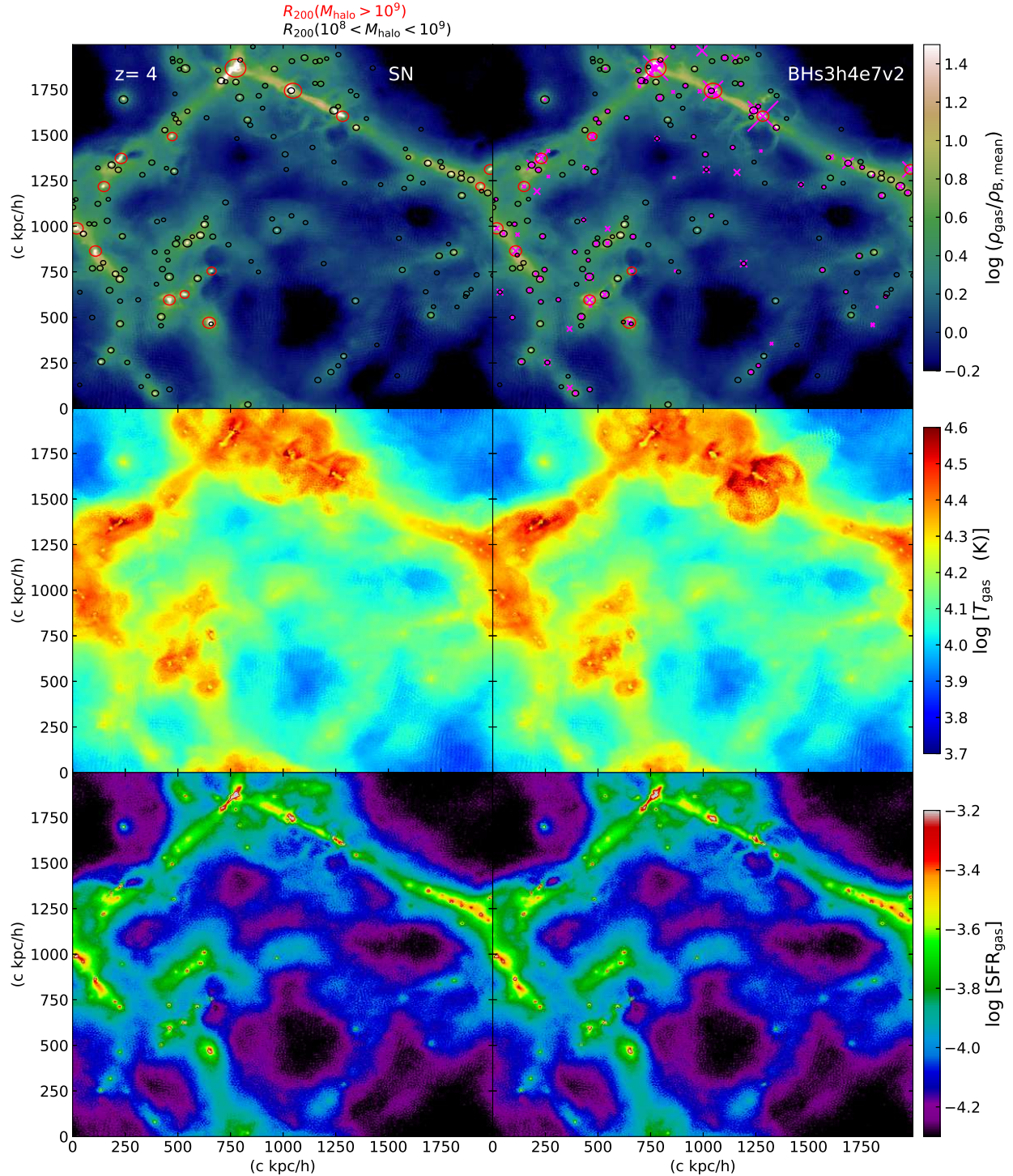


**Figure 1.** Gas properties (2D projection integrated over the third Cartesian direction) in the whole  $(2000h^{-1} \text{ kpc})^3$  simulation box at  $z = 4$ , with the three rows presenting: overdensity (first row – top), temperature (second), and SFR (third – bottom). The two columns are for different simulations: *SN* (left) and *BHs3h4e7v2* (right). The red circles in the top row depict the virial radius  $R_{200}$  of galaxies in the mass range  $M_{\text{halo}} > 10^9 M_{\odot}$ , while the black circles show the  $R_{200}$  of  $10^8 < M_{\text{halo}} < 10^9 M_{\odot}$  galaxies. The positions of BHs in run *BHs3h4e7v2* are indicated by the magenta cross-points in the top-right panel, where the symbol size is proportional to BH mass.

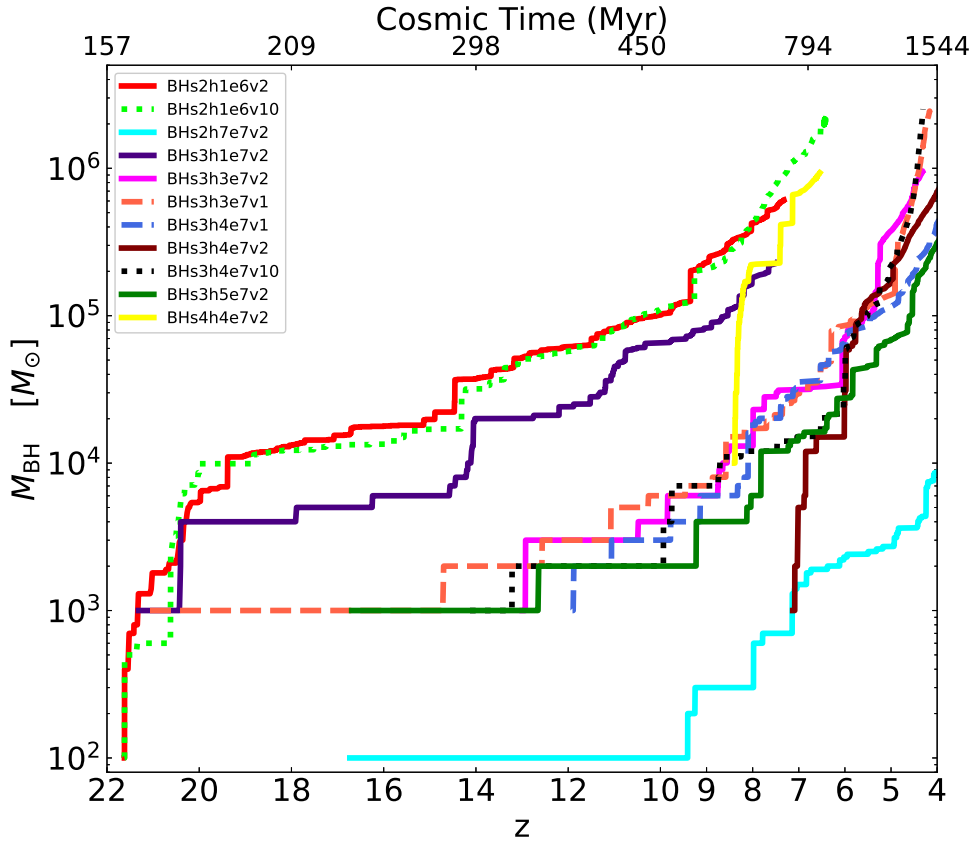


**Figure 2.** BH mass growth with redshift of the most-massive BH in each run. The different colours and linestyles discriminate the runs as labelled, which are: *BHs2h1e6v2* - red solid curve, *BHs2h1e6v10* - lime-green dotted, *BHs2h7e7v2* - cyan solid, *BHs3h1e7v2* - indigo solid, *BHs3h3e7v2* - magenta solid, *BHs3h3e7v1* - light-red dashed, *BHs3h4e7v1* - blue dashed, *BHs3h4e7v2* - maroon solid, *BHs3h4e7v10* - black dotted, *BHs3h5e7v2* - green solid, and *BHs4h4e7v2* - yellow solid.

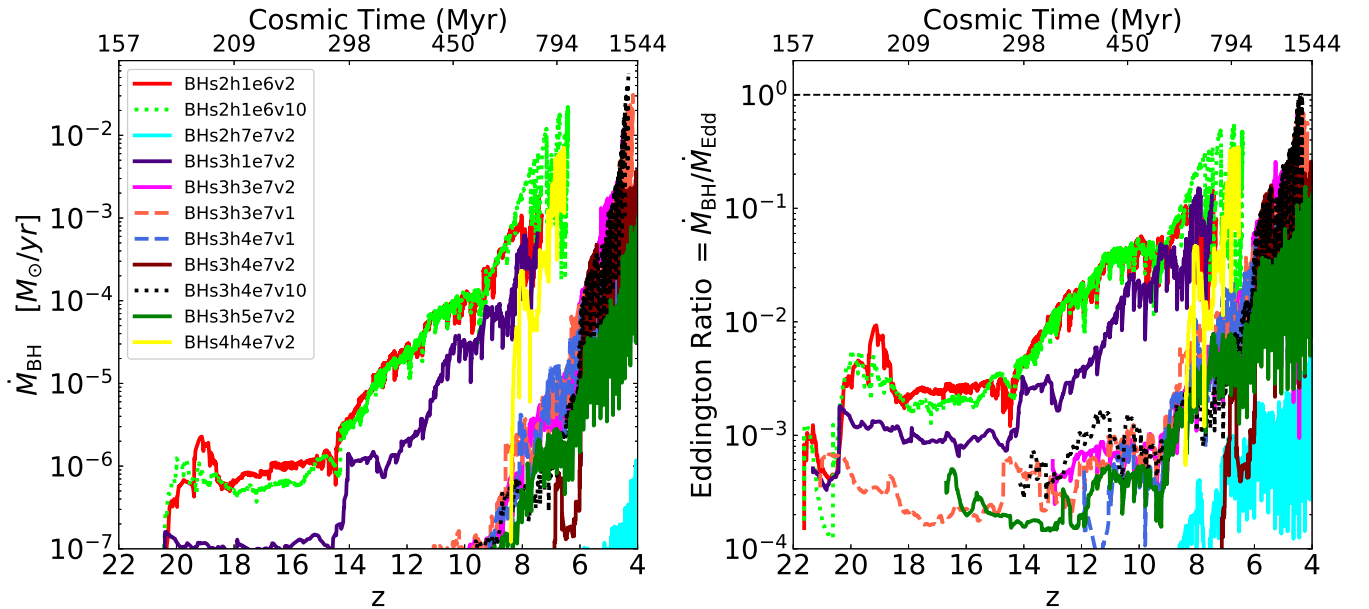


**Figure 3.** BH accretion rate (left panel) and Eddington ratio (right panel) growth with redshift of the most-massive BH in each run.

cretion rate ( $\dot{M}_{\text{BH}}$ ) in the left panel, and Eddington ratio  $= \dot{M}_{\text{BH}}/\dot{M}_{\text{Edd}}$  at the right. There is variability of the  $\dot{M}_{\text{BH}}$ , whereby it fluctuates by a factor of up to 100. In the beginning, when the BHs are just seeded, they are accreting at highly sub-Eddington rates with Eddington ratio  $< 0.0001 - 0.001$ . The accretion rate grows with time as the BHs grow in mass, and the gas density in the BH vicinity increases by cosmic gas inflow to galaxy centers.

We note that the growth of a BH is initially dominated by mergers with other BHs soon after its seeding for about a 100 to 200 Myr, when  $\dot{M}_{\text{BH}} < \sim 0.05\dot{M}_{\text{Edd}}$ . Growth by gas accretion dominates at later times, when the Eddington ratio is larger. Such a trend was also found for SMBH growth in Barai et al. (2018). In some of our simulations, the BHs continue to grow at much later times, even when star formation has started to be quenched. This occurs due to gas inflows driven by galaxy mergers and galaxy tidal encounters (further discussed in §3.5.2).

We find that the massive BHs grow to  $M_{\text{BH}} =$  a few  $\times 10^5 - 10^6 M_{\odot}$  by  $z = 5$  in most of our simulations (red solid, lime-green dotted, indigo solid, magenta solid, light-red dashed, blue dashed, maroon solid, black dotted, green solid, and yellow solid curves). The accretion rate of these massive BHs has grown to  $\dot{M}_{\text{BH}} = (0.2-1)\dot{M}_{\text{Edd}}$ . The exception is the case where BHs of the smallest seed ( $10^2 M_{\odot}$ ) are placed in the largest halos ( $7 \times 10^7 M_{\odot}$ ) (run *BHs2h7e7v2*, cyan solid curve), where the most-massive BH grows up to  $M_{\text{BH}} = 10^4 M_{\odot}$  only. For this BH, gas accretion is always occurring at low Eddington ratios ( $\dot{M}_{\text{BH}} \leq 0.01\dot{M}_{\text{Edd}}$ ).

The final BH properties reached at  $z = 4$  depend on the simulation. E.g., in run *BHs3h3e7v1* (light-red dashed curve):  $M_{\text{BH}} = 2 \times 10^6 M_{\odot}$  and  $\dot{M}_{\text{BH}} = 0.02 M_{\odot}/\text{yr}$ . In Table 2 we list the final BH mass and the accretion rate range (maximum and minimum over the final 50 Myr period) of the most-massive BH, together with the final redshift of each simulation run.

We note that some simulations were stopped before  $z = 4$ . These are the runs where star-formation is already quenched at a high- $z$ . To optimize our finite computational resources, once significant quenching of SF were already achieved by the growing BHs at a higher- $z$ , we did not continue those simulations further.

The left panel of Fig. 4 shows the total BH Accretion Rate Density (BHARD) as a function of redshift. Each curve is for one run, labelled by the different colours and linestyles. The BHARD (in  $M_{\odot} \text{ yr}^{-1} \text{ Mpc}^{-3}$ ) is computed by summing over the accretion rate of all the BHs inside each simulation box at a time, and dividing it by the box volume. We find an overall similar behaviour of the most-massive BH accretion rate (Fig. 3), and the total BHARD in the simulation volume (Fig. 4). This is because the relative accretion rate trends between simulations remain the same when considering one BH or multiple BHs. In other words, all the BHs in a simulation behave similarly in this regard. E.g. if the  $\dot{M}_{\text{BH}}$  of the most-massive BH in a run is higher than the most-massive  $\dot{M}_{\text{BH}}$  of another run, then the BHARD is also higher in the former case, because it will have several BHs whose  $\dot{M}_{\text{BH}}$  are higher than in the 2nd run.

### 3.3 Star Formation Rate

Stars form in the simulation volume from cold dense gas. Fig. 4 exhibits the global Star Formation Rate Density (SFRD) as a function of redshift, for all the simulations labelled by the different colours and linestyles. The SFRD (in  $M_{\odot} \text{ yr}^{-1} \text{ Mpc}^{-3}$ ) is computed by summing over all the SF occurring in each simulation box at a time, and dividing it by the time-step interval and the box volume. Observational data ranges are shown, for a comparison, as the grey shaded region, taken mainly from Cucciati et al. (2012), and the compilations therein originally from Perez-Gonzalez et al. (2005), Schiminovich et al. (2005), Bouwens et al. (2009), Reddy & Steidel (2009), Rodighiero et al. (2010), van der Burg, Hildebrandt & Erben (2010), Bouwens et al. (2012). We note that the observational data are mostly based on massive galaxies. The SFRD as indicated by these observations continues to grow at  $z < 6$ , and has a peak around  $z = 2$  which is due to the brightest galaxies (Cucciati et al. 2012). This implies that significant gas reservoirs exist in such more massive galaxies at these epochs, and are being replenished by cosmic accretion and galaxy mergers. While quenching processes due to BH and SN driven outflows/feedback are still less strong to lower the SF in these galaxies at  $z \sim 2 - 3$ .

In our simulations of the formation of dwarf galaxies, we see that the SFRD rises with time from early epochs  $z \sim 15$ , and all the runs behave similarly up to  $z \sim 9$ . Most of the simulations reach a maximum SFRD in the form of a plateau between  $z = 4 - 6$ , and the SFRD decreases at  $z > 6$  and at  $z < 4$ . The scenario changes completely at  $z < 8$  if we consider no BH or SN feedback (see Fig. 8 and §3.5.1). In the absence of any feedback, the SFRD continues to grow until recent epochs overshooting the observational limits (more details in §3.5.1).

Back to Fig. 4, we consider the *SN* run (dark blue curve) without BHs as the baseline, and compare other simulations with it to estimate the impact of BH feedback. The SFRD in simulation *BHs2h7e7v2* (cyan solid curve) is almost similar to that in the run *SN*, because the BHs are too small there to generate enough feedback. A similar outcome happens in the other runs at  $z \geq 9$ , when the BHs are too small.

Star formation mostly occurs over an extended region at galaxy centres, where cosmic large-scale-structure gas inflows and cools. The presence of a central BH helps to quench star formation, because a fraction of dense gas is accreted onto the BH, and a fraction is ejected out by BH feedback. The processes of BH accretion and feedback contribute to suppress SF substantially in most of the runs, from  $z \sim 9$  onwards, when the BHs have grown massive and generate larger feedback energy. Compared to the *SN* case (dark blue curve), the SFRD is reduced by a factor of several in most of the other runs at  $z < 9$ .

We find that BH accretion and feedback causes a quenching of the SFRD at cosmic epochs  $z \leq 9$ , by factors 1.1 – 3 times reduction. The precise redshifts and suppression factors are given in the following for the different simulations (with the same BH outflow velocity  $v_w = 2000$  km/s):

- *BHs2h1e6v2* (red solid curve in Fig. 4) at  $z \leq 9$  up to 2 times reduction of SFRD,

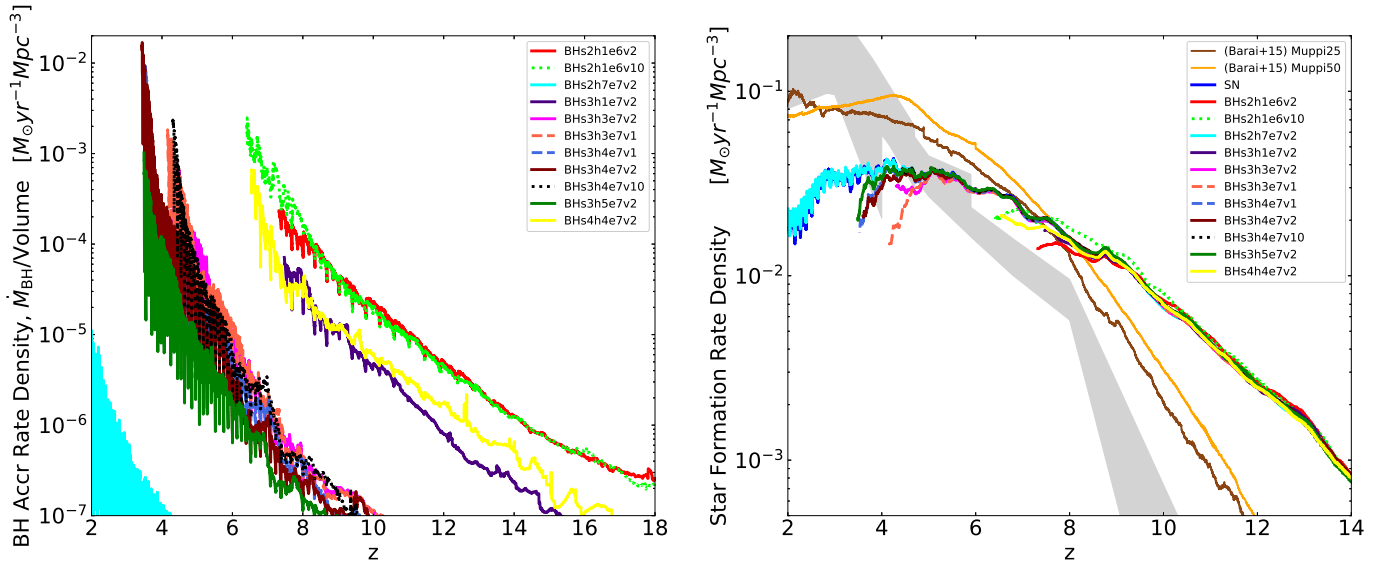


**Figure 4.** Total BH accretion rate density (left panel), and star formation rate density (right panel) integrated over the whole simulation volume as a function of redshift, with the different models labelled by the colours and linestyles. For comparison in the right panel, the brown and orange thinner curves show two models from Barai et al. (2015), which are SFRD results for more massive galaxy formation/evolution, from larger volume cosmological simulations. The grey shaded region denotes a combination of observational SFRD data range from Cucciati et al. (2012), and the compilations therein originally from Perez-Gonzalez et al. (2005), Schiminovich et al. (2005), Bouwens et al. (2009), Reddy & Steidel (2009), Rodighiero et al. (2010), van der Burg, Hildebrandt & Erben (2010), Bouwens et al. (2012).

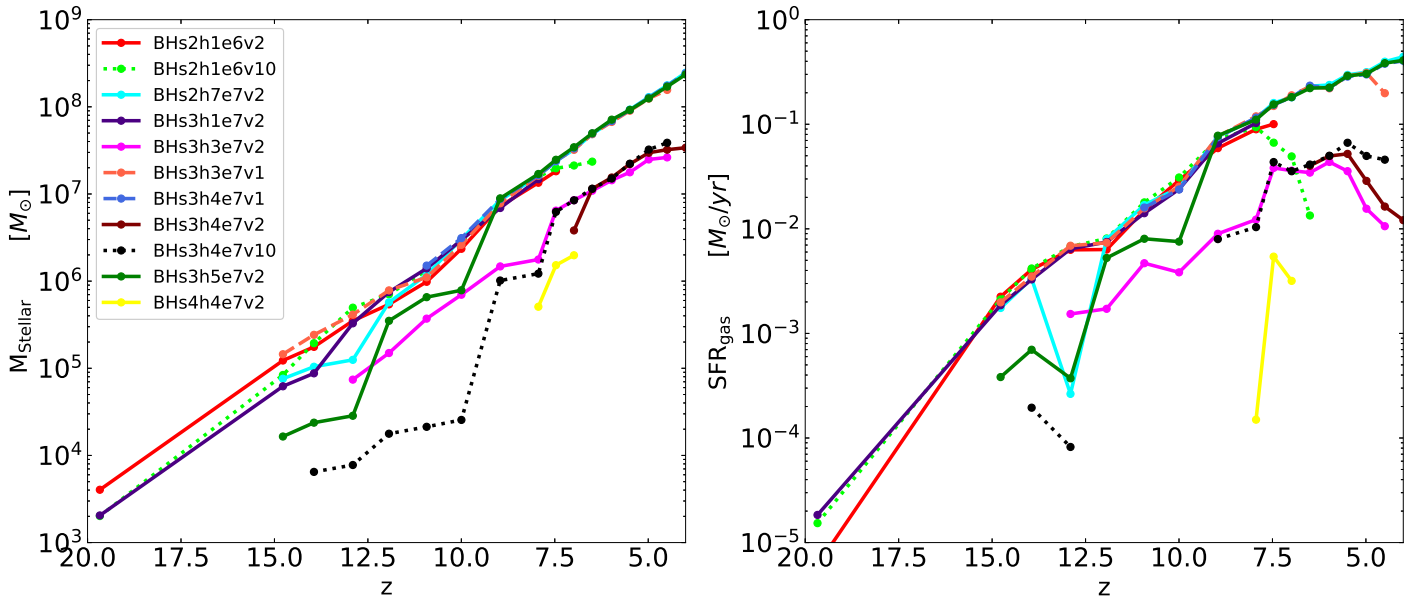


**Figure 5.** Stellar mass (left panel) and total star formation rate (right panel) evolution with redshift of the galaxy hosting the most-massive BH in each run.

**Table 2.** Final black hole mass and accretion rate range of the most-massive BH for the different simulation runs.

Run name	Final Redshift	BH mass, $M_{\text{BH}}[M_{\odot}]$	BH accretion rate, $\dot{M}_{\text{BH}}[M_{\odot}/\text{yr}]$ (maximum and minimum over the final 50 Myr period)
<i>BHs2h1e6v2</i>	7.5	$6 \times 10^5$	0.001 – 0.002
<i>BHs2h1e6v10</i>	6.5	$3 \times 10^6$	0.0002 – 0.03
<i>BHs2h4e7v2</i>	4.2	$2 \times 10^4$	$6 \times 10^{-7} - 10^{-5}$
<i>BHs2h7e7v2</i>	4	$1 \times 10^4$	$10^{-7} - 10^{-6}$
<i>BHs3h1e7v2</i>	7.5	$3 \times 10^5$	0.0002 – 0.0007
<i>BHs3h2e7v2</i>	6.2	$3.5 \times 10^5$	0.0007 – 0.001
<i>BHs3h3e7v2</i>	4.2	$8 \times 10^5$	0.003 – 0.015
<i>BHs3h3e7v1</i>	4.2	$3 \times 10^6$	0.002 – 0.03
<i>BHs3h4e7v1</i>	4	$4 \times 10^5$	0.0005 – 0.002
<i>BHs3h4e7v2</i>	4	$4 \times 10^5$	0.0002 – 0.004
<i>BHs3h4e7v5</i>	4	$2 \times 10^6$	0.005 – 0.03
<i>BHs3h4e7v10</i>	4.2	$3 \times 10^6$	0.003 – 0.06
<i>BHs3h5e7v2</i>	4	$3 \times 10^5$	$6 \times 10^{-5} - 0.0008$
<i>BHs4h4e7v2</i>	6.5	$1 \times 10^6$	0.0015 – 0.008

- *BHs3h1e7v2* (indigo solid curve) at  $z \leq 8$  up to 1.1 times,
- *BHs4h4e7v2* (yellow solid curve) at  $z \leq 8$  up to 2 times,
- *BHs3h2e7v2* at  $z \leq 7$  up to 1.5 times,
- *BHs3h3e7v2* (magenta solid curve) at  $z \leq 5$  up to 2 times,
- *BHs3h4e7v2* (maroon solid curve) at  $z \leq 4.5$  up to 3 times,
- *BHs3h5e7v2* (green solid curve) at  $z \leq 4.2$  up to 3 times.

Thus, we find that BHs need to grow to a mass  $M_{\text{BH}} \sim$  a few times  $10^5 M_{\odot}$ , in order to suppress star-formation in dwarf galaxies (of  $M_{\star} = 10^5 - 10^8 M_{\odot}$ ).

A larger BH outflow velocity ( $v_w$ ) does not change the results substantially. E.g., comparing the red solid and lime-green dotted curves in Fig. 2, the BH mass growth remains almost the same with  $v_w = 2000$  and  $10000$  km/s. Increasing  $v_w$  decreases the mass outflow rate ( $\dot{M}_w$  in Eq.(8)), in the way favoring an increase in the BH accretion rate, as we see in Fig. 3 at late epochs (comparing red solid and lime-green dotted curves at  $z < 9$ ). Further, the smaller mass outflow rate to the environment delays the suppression of star formation (comparing lime-green dotted and red solid curves in Fig. 4).

Fig. 5 displays the stellar properties as a function of redshift of the galaxy hosting the most-massive BH in each run (labelled by its colour and linestyle): stellar mass ( $M_{\star}$  in units of  $M_{\odot}$ ) in the left panel, and total star formation rate in the right panel. The total SFR (in  $M_{\odot}/\text{yr}$ ) is computed by summing over all the SF in gas particles occurring inside the galaxy virial radius  $R_{200}$  (defined in Eq. 11).

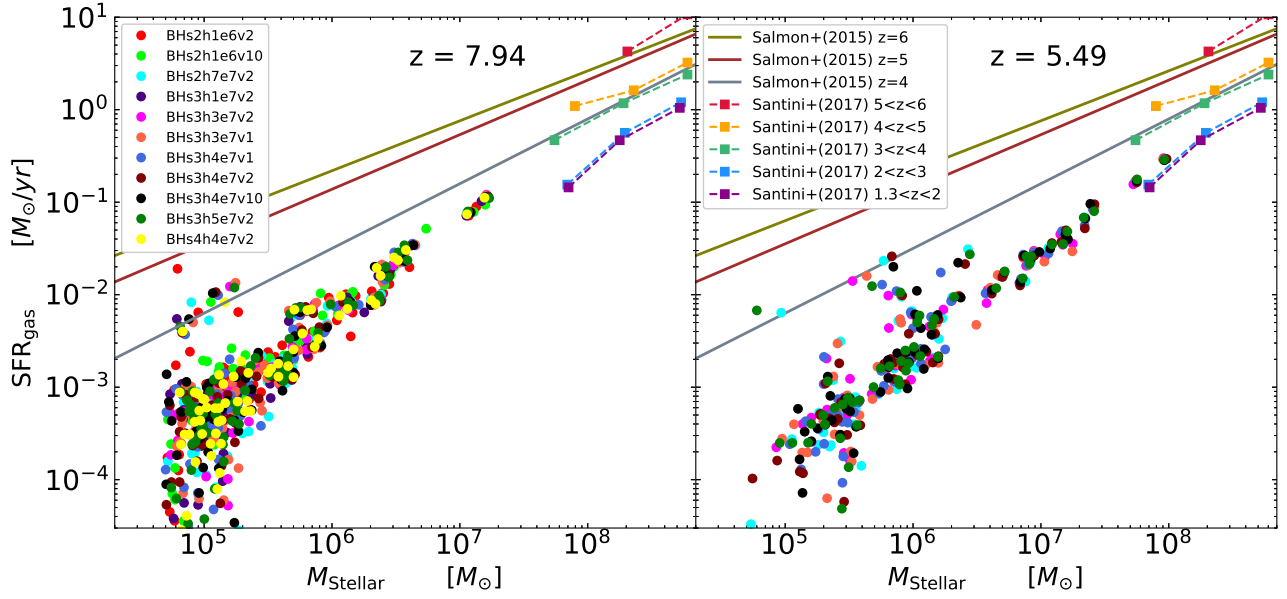
We see that the SFR of the galaxy hosting the most-massive BH behaves similarly overall as the global SFRD (presented in Fig. 4 - right panel). The SFR continues to increase (with no quenching) in the simulation *BHs2h7e7v2* (cyan solid curve), because there the BHs are too small to generate enough feedback. A similar non-quenching of SFR is also seen in run *BHs3h5e7v2* (green solid curve), where the BH mass at  $z = 4$  is smaller than all the runs. For the other simulations, there is a quenching of SFR in the galaxies by their centrally growing BHs. This can be visualised by the anti-correlation: SFR in Fig. 5 reduces when the BH mass has a corresponding sharp growth in Fig. 2.

Fig. 6 presents the SFR (in  $M_{\odot}/\text{yr}$ ) versus stellar mass ( $M_{\star}$ ) of all the galaxies within the cosmological boxes, at the epoch  $z = 7.94$  in the left panel, and  $z = 5.49$  in the right. The filled circles are our simulation results, with the plotting colours distinguishing results from different runs. Observational data is overplotted as the solid and dashed lines indicating the SFR versus  $M_{\star}$  relationships at different epochs. The solid lines indicate observations from Salmon et al. (2015) of star-forming galaxies at  $z = 4, 5, 6$ : the best-fit relation of SFR versus  $M_{\star}$  as written in their Equation (6) with parameters given in their Table 4. Note that the fit was done on more massive galaxies, but here the same relation has been extended to lower masses. The dashed lines show observations from Santini et al. (2017) in different redshift bins within  $z = 1.3 - 6$ : the data points are taken from their Table 1, and here only the average data with  $M_{\star} < 10^9 M_{\odot}$  are shown as the square plotting symbols.

We find that our simulated DGs exhibit a positive SFR versus  $M_{\star}$  correlation qualitatively similar to the observations, but with an offset in the [SFR -  $M_{\star}$ ] plane. Most of our DGs are consistent with the relations showing the observational main sequence of star-forming galaxies, when extrapolated to lower masses. There is a large scatter in our SFR versus  $M_{\star}$  correlation, going up to 1 dex at the lowest masses. Some of our low-mass ( $M_{\star} \sim 10^5 - 10^6 M_{\odot}$ ) and high-SFR (SFR  $\sim 0.003 - 0.03 M_{\odot}/\text{yr}$ ) galaxies fall on the  $z \sim 4$  relation of Salmon et al. (2015) and Santini et al. (2017). At  $z = 5.49$  (right panel of Fig. 6), our galaxies lie on the  $z \sim 2$  relation of Santini et al. (2017). Whereas at  $z = 7.94$  (left panel), our galaxies lie between the  $z \sim 2$  and  $z \sim 4$  relations of Santini et al. (2017).

### 3.4 Black Hole - Galaxy Correlation

The BH - galaxy correlation obtained in our simulations is presented in Fig. 7 as the  $M_{\text{BH}}$  versus  $M_{\star}$  (stellar mass) diagram. It shows all the galaxies within the simulation volume with  $M_{\star} > 10^{4.5} M_{\odot}$ , at two epochs:  $z = 7.94$  in the left panel, and  $z = 5.49$  in the right panel. The plotting colour distinguishes results from different runs. Observational data is overplotted as the black lines indicating the



**Figure 6.** SFR versus stellar mass of the galaxies within the simulation volume, at the epoch  $z = 7.94$  in the left, and  $z = 5.49$  in the right panel. The filled circles are our simulation results, with the plotting colours distinguishing results from different runs. The lines indicate observational results of SFR versus stellar mass relation for: star-forming galaxies at  $z = 4, 5, 6$  (Salmon et al. 2015) as the solid lines, and galaxies in different redshift bins within  $z = 1.3 - 6$  (Santini et al. 2017) as the dashed lines with square plotting symbols.

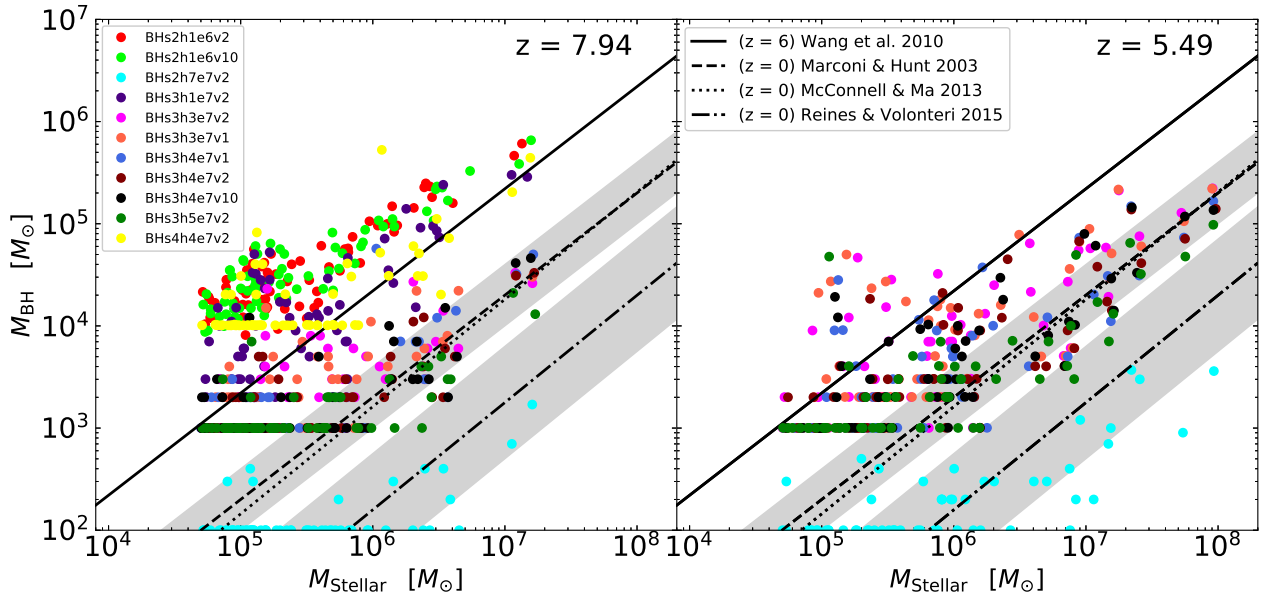


**Figure 7.** BH mass versus stellar mass of the galaxies within the simulation volume, at two epochs  $z = 7.94, 5.49$ , in the two panels. The plotting colours distinguish results from different runs. The black lines indicate the observed BH mass versus galaxy stellar mass relation for:  $z \sim 6$  quasars (Wang et al. 2010) as the solid line, and local galaxies (Reines & Volonteri 2015) as the dash-dotted line, showing the correlation with the bulge mass as the dashed (Marconi & Hunt 2003) and dotted (McConnell & Ma 2013) lines.

BH mass versus stellar bulge mass relationships at different epochs. Local galaxies ( $z = 0$ ) are represented by the black-dashed line:  $M_{\text{BH}}/M_{\star} = 0.002$  (Marconi & Hunt 2003), as well as from Reines & Volonteri (2015) as the dash-dotted line, and from McConnell & Ma (2013) as the dotted line. The ratio is observed to be steeper at high- $z$ . Far-IR and CO bright  $z \sim 6$  quasars lie along the black-solid line: median  $M_{\text{BH}}/M_{\star} = 0.022$  (Wang et al. 2010).

We find a huge scatter in the  $[M_{\text{BH}} - M_{\star}]$  correlation of the simulated galaxies, especially at low- $M_{\star}$ . In our simulations *BHs2h1e6v2* (red symbols in Fig. 7) and *BHs3h1e7v2* (indigo symbols), dwarf galaxies with stellar masses between  $M_{\star} = 10^4 - 10^7 M_{\odot}$  contain BHs in the range  $M_{\text{BH}} = 10^3 - 10^5 M_{\odot}$  at  $z = 7.9$ , which are hence already more massive than BHs following the local relation, as well as BHs in  $z \sim 6$  quasars. These two are also the runs where SF quenching happens the earliest, implying that the suppression occurs due to BH activities.

BHs in the simulation *BHs4h4e7v2* (yellow symbols in Fig. 7) fall on the observed  $z \sim 6$  relation of  $[M_{\text{BH}} - M_{\star}]$  already at  $z = 7.9$ . In the run *BHs3h2e7v2*, BHs lie in between the two correlations at  $z = 7.9$ , and have migrated to the  $z \sim 6$  relation at the later epoch. Central BHs in the runs *BHs3h3e7v2* (magenta symbols), *BHs3h4e7v2* (maroon symbols), and *BHs3h5e7v2* (green symbols) more or less follow the local  $z = 0$  correlation at both the epochs plotted; although their scatter increases substantially in the right panel. When BHs do not grow much (run *BHs2h7e7v2*, cyan symbols, most-massive reaching  $M_{\text{BH}} < 10^4 M_{\odot}$  only), they always lie significantly below both of the  $[M_{\text{BH}} - M_{\star}]$  correlations.

At the same time, there are studies (e.g., Volonteri & Natarajan 2009, using semi-analytical models), which find that the existence of the  $[M_{\text{BH}} - \sigma]$  correlation is purely a reflection of the merging hierarchy of massive dark matter haloes.

We find that there is a direct connection between early BH growth and the quenching of SF, which is henceforth caused by resulting BH feedback. In addition, our results of fast BH growth at the centers of dwarf galaxies suggest that these BHs grow faster than their host galaxies in the early Universe.

### 3.5 Varying the SN Feedback

We now check the impact of supernovae feedback strength on our results, by varying the mass loading factor  $\eta$  of SN wind kinetic feedback (§2.1). So far, we have discussed only simulations with the same SN feedback, using a default value of  $\eta = 2$  (e.g., Tescari et al. 2011; Barai et al. 2015). This corresponds to  $\chi = 0.27$  ( $\chi$  defined in Eq. (2) of §2.1) of SN energy being carried away by the wind. We now consider a new run with a stronger SN-driven mass ejection. This simulation *BHs3h1e7v2-SNhi* has a higher  $\eta = 5$ , while the other parameters are the same as *BHs3h1e7v2*. In this new run,  $\chi = 0.67$  of SN energy is carried away by the wind, which is a high value for the SN feedback efficiency.

#### 3.5.1 Impact of SN Feedback Strength on SFR

Fig. 8 displays the global Star Formation Rate Density as a function of redshift, for the simulations with different

strengths of SN feedback. The SFRD rises with time as more and more stars form from available gas. The simulation *noSN-noBH* (green dashed curve) with no SN feedback and no BH accretion/feedback, has no source to deplete the gas, and the SFRD continues to rise in this run up to  $z = 3$ , overshooting the observational limits. Feedback processes from SN and BH suppress SF substantially in the other runs at  $z < 10$ .

Comparing the cases *noSN-noBH* (green dashed) and *SN* (dark blue solid), we find that SN feedback quenches SF by 10 – 100 times at  $z < 6$ . While the quenching by BH feedback (§3.3) is to reduce the SFRD by factors 1.1 – 3 only. When the SN feedback strength is increased to  $\eta = 5$  (simulation *BHs3h1e7v2-SNhi*, red dashed curve), the SFRD is lowered by a factor 2 from  $z = 10$  compared to run *BHs3h1e7v2* (indigo solid).

Thus, we find that SN feedback quenches star-formation by a larger factor than the quenching by BH feedback. This result of ours is in agreement with several other galaxy simulation studies (e.g., Dubois et al. 2015; Habouzit et al. 2017; Angles-Alcazar et al. 2017; Prieto et al. 2017; Trebitsch et al. 2018).

#### 3.5.2 Impact of SN Feedback Strength on BH Growth

The growth of the most-massive BH in runs *BHs3h1e7v2-SNhi* and *BHs3h1e7v2* are plotted in Fig. 9: redshift evolution of BH mass in the left panel, and accretion rate Eddington ratio at the right. The BH properties remain more-or-less the same in both simulations. After being seeded at  $z \sim 21$  as  $10^3 M_{\odot}$  BHs, they grow in mass by accreting dense gas from their surroundings and by merger with other BHs, to  $M_{\text{BH}} = 3 \times 10^5 M_{\odot}$  by  $z \sim 7$ . The accretion rate grows as well similarly from Eddington ratio  $< 0.0001$  at seeding, to  $\dot{M}_{\text{BH}} \sim 0.2 \dot{M}_{\text{Edd}}$  by  $z \sim 7$ , with substantial variability of the  $\dot{M}_{\text{BH}}$  at later epochs.

Thus, we find that in our simulations varying SN feedback has a little impact on BH growth. Our BHs continue to grow up to  $z \sim 6$  even in the presence of stronger SN-driven mass ejection. We note that this result is contrary to some recent zoomed-in cosmological hydrodynamical simulation studies (e.g., Dubois et al. 2015; Angles-Alcazar et al. 2017; Prieto et al. 2017; Trebitsch et al. 2018) which find that strong SN feedback hampers BH growth, by removing gas from around the BH. Simulating a  $10^{12} M_{\odot}$  halo, Dubois et al. (2015) found that at  $z > 3.5$  efficient feedback from SN destroys dense cold gas clumps at the galaxy core, preventing early BH growth. However later on, BH growth occurs from gas inflows induced by major mergers of galaxies. Simulating  $10^{12.5} M_{\odot}$  haloes down to  $z = 1$ , Angles-Alcazar et al. (2017) showed that early BH growth is limited by bursty stellar feedback evacuating gas from galactic nuclei. Simulating a  $3 \times 10^{10} M_{\odot}$  halo down to  $z = 6$ , Prieto et al. (2017) showed that, in the absence of SN feedback, AGN feedback alone does not affect significantly either SF or BH growth. Performing zoom-in radiation hydrodynamics simulations of a  $5 \times 10^9 M_{\odot}$  halo down to  $z = 5.7$ , Trebitsch et al. (2018) found that SN feedback prevents the growth of the BH, thus quenching its associated feedback.

In another study, Habouzit et al. (2017) performed periodic (10 Mpc)<sup>3</sup> simulations up to  $z = 2$ , using a new implementation of BH seed formation in low-metallicity environ-

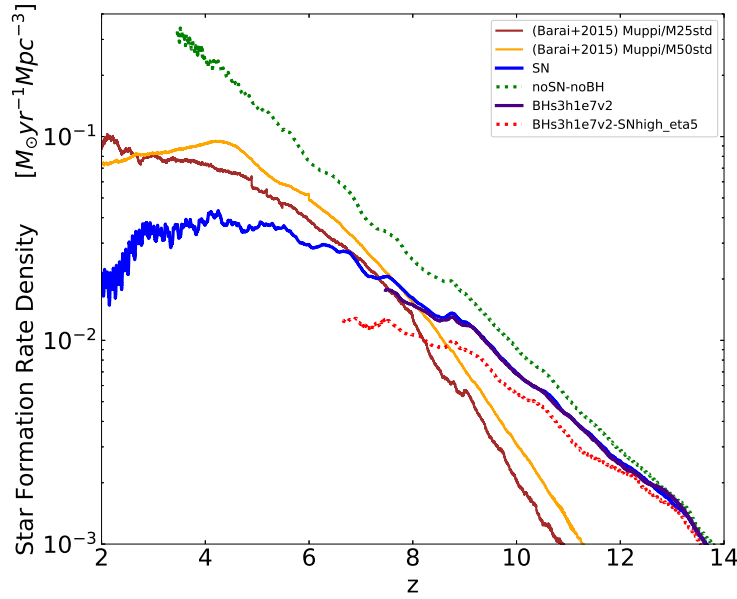


**Figure 8.** Total star formation rate density as a function of redshift, in the simulations with different strengths of SN feedback. The colours and linestyles discriminate the runs as labelled, *noSN-noBH* : green dashed, *SN* : dark blue solid, *BHs3h1e7v2* : indigo solid, and *BHs3h1e7v2-SNhi* : red dashed. For comparison, the brown and orange thinner curves show two models from Barai et al. (2015), which are SFRD results for more massive galaxy formation/evolution, from larger volume cosmological simulations.

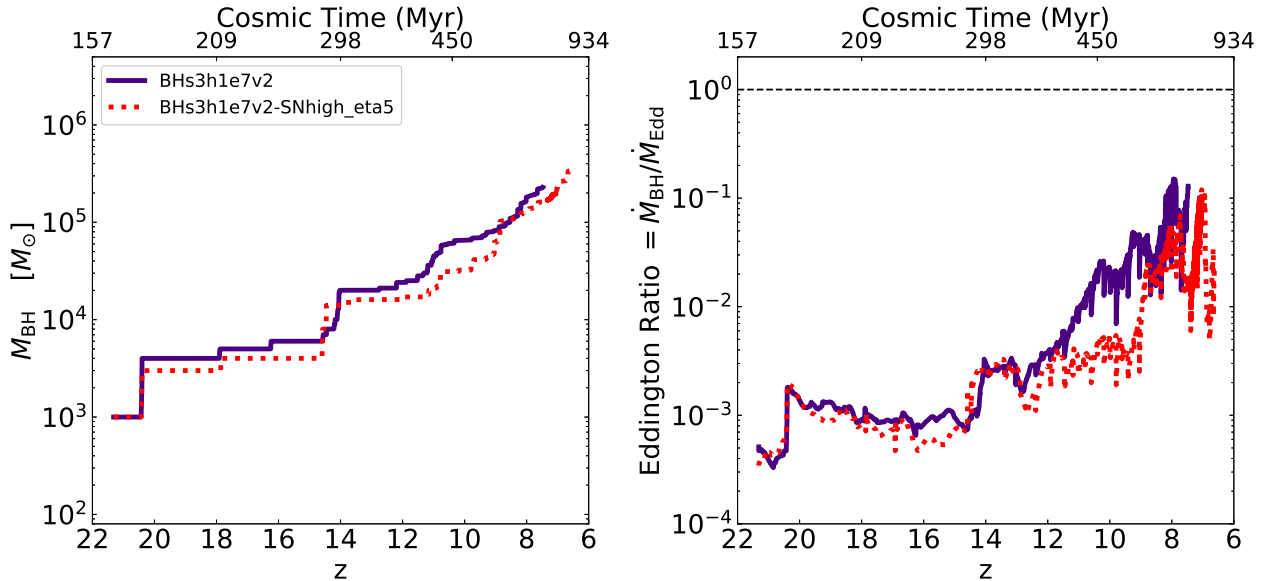


**Figure 9.** BH mass (left panel) and BH accretion rate Eddington ratio (right panel) growth with redshift in two runs with different strengths ( $\eta$ ) of SN feedback. The colours discriminate the runs as labelled, which are: *BHs3h1e7v2* - indigo solid, and *BHs3h1e7v2-SNhi* - red dashed.

ments, and found that all high-mass galaxies tend to host a BH, while low-mass galaxies have a lower probability of hosting a BH. In Dubois et al. (2015) and Habouzit et al. (2017), the BH growth is hampered by strong SN feedback, only for their delayed cooling SN feedback implementation where gas cooling is turned off for a certain duration. Thus

the numerical formulation of the relevant physical processes can contribute to obtaining different results in the simulations.

We remind below some features in our sub-resolution models which lead to the SN feedback being less coupled to the galaxy ISM. In our simulations, newly kicked SN wind

particles are decoupled from hydrodynamic interactions (as described in §2.1, last paragraph). This is done in order to create SN outflows without destroying dense star forming regions. It allows SN winds to travel until reaching a density  $\rho_{\text{dec}} = 0.25\rho_{\text{SF}} = 0.03 \text{ cm}^{-3}$  (number density of hydrogen atoms), before being hydrodynamically coupled again. Although widely used, this implementation effectively allows SN winds to escape the galaxy, while decoupled from the ISM. So even though we have increased the mass loading factor of SN kinetic feedback in the new run *BHs3h1e7v2-SNhi*, it does not necessarily mean that the coupling between the SN feedback and the ISM is stronger, because of the hydrodynamic decoupling feature present. Also note that our SN wind particles are kicked in a direction  $+$  or  $-$  ( $\vec{v}_{\text{old}} \times \vec{\nabla}\phi$ ) (§2.1, fifth paragraph), with an aim to create SN outflows preferentially ejected perpendicular to the galaxy disk. Such a prescription reduces even more the coupling between SN feedback and the ISM of the galaxy.

Given the above aspects of our SN outflow sub-resolution scheme, it can be unexpected to find that our star formation is strongly quenched by SN feedback (§3.5.1), higher than the quenching by BH feedback. This can probably be explained by the low value of the star-formation threshold density used (§2.1, second paragraph):  $\rho_{\text{SF}} = 0.13 \text{ cm}^{-3}$ . As a result, even the diffuse gas in the galaxy is considered as star forming, and will be the most affected by SN feedback.

Hence to summarize, the apparent discrepancy of our result (continued BH growth) with the other studies in the literature is because of several conditions: environmental effects and our cosmological setup, combined with the different numerical implementation of the sub-resolution physical processes. We have smaller BHs in smaller halos, but in a full cosmological environment; therefore the effects of galaxy mergers and hierarchical structure formation should be fully taken into account. In our simulations, the supply of gas is maintained for a longer time, so that BHs can grow even in the presence of stronger SN feedback. As galaxies assemble in a cosmological environment, there are gas inflows to centers driven by major/minor galaxy mergers, tidal encounters, galaxy harassment etc. This sustained accumulation of gas flows over longer time periods enable the central BHs to grow. Such a conclusion of late BH growth was also implied by Dubois et al. (2015).

Earlier we discussed our finding that the accretion rate  $\dot{M}_{\text{BH}}$  of the growing BHs is highly variable (Fig. 3 in §3.2, and Fig. 9 - right panel in §3.5.2). A possible reason for this phenomenon is self-regulation by the feedback from BHs and/or supernova. A cycle of accretion-induced inflow is followed by BH- and/or SN-driven feedback-induced outflow, which makes the gas supply intermittent. At the same time, gas supply is not depleted in the long term. The inflow-outflow cycles continue up to  $z \sim 4$ , and the BHs grow during inflows.

Note that Habouzit et al. (2017) also performed fully cosmological simulations, however found that SN feedback prevents BH growth in low-mass galaxies, but only when using a more efficient SN feedback sub-resolution recipe.

In a recent study, Koudmani et al. (2018) performed high-resolution isolated DG simulations, using a constant BH accretion rate equal to a fixed fraction of the Edington rate based on the initial BH mass. Thus mimick-

ing a maximal feedback effect, they found that AGN outflows have a small but systematic effect on the galaxy central SFRs. While significant effects on the global SFR are only obtained with strong SN feedback and sustained high-luminosity isotropic AGN winds. The outflows reach much higher velocities and much-higher temperatures with AGN feedback included.

## 4 SUMMARY AND CONCLUSIONS

Intermediate-Mass Black Holes (with masses between  $100 - 10^6 M_{\odot}$ ) have historically been an elusive population of BHs, compared to the stellar-mass and supermassive (widely observed at the centers of AGN) BH counterparts. Recently these IMBHs have started to be observed in low-mass galaxies. Our work focuses on the case that IMBHs are formed at the centers of dwarf galaxies. Early feedback from such IMBHs is expected to release energy and affect the host gas-rich dwarf galaxies at  $z = 5 - 8$ , quenching star-formation, reducing the number of DGs, and impacting the density profile at DG centers. This can possibly solve several anomalies in the dwarf galaxy mass range within the concordance  $\Lambda$ CDM cosmological scenario of galaxy formation (Silk 2017).

We have investigated the growth and feedback of IMBHs at DG centers, by performing cosmological hydrodynamical simulations. We have employed a modified version of the SPH code GADGET-3. It includes the following sub-resolution physics: radiative cooling and heating from a photoionizing background, star-formation, stellar evolution, chemical enrichment for 11 elements, supernova feedback, AGN accretion and feedback. We simulated  $(2h^{-1} \text{ Mpc})^3$  comoving volumes to probe dwarf galaxies at high redshifts. The mass resolutions are  $3.44 \times 10^4 h^{-1} M_{\odot}$  for dark matter particles, and  $6.43 \times 10^3 h^{-1} M_{\odot}$  for gas particles. The length resolution is  $0.1h^{-1} \text{ kpc}$  comoving which is the gravitational softening length. The cosmological boxes are evolved with periodic boundary conditions, from  $z = 100$  up to  $z = 4$ .

We executed a series of simulations: one of them is a control case with SF-only and no BH; the other runs include BHs and explore different parameter variations of the BH sub-resolution models. In particular, we seed BHs of mass:  $M_{\text{BHseed}} = (10^2, 10^3, 10^4) M_{\odot}$ , at the centers of massive halos with  $M_{\text{halo}} > M_{\text{HaloMin}} = (10^6 - 5 \times 10^7) M_{\odot}$ . In addition to  $M_{\text{HaloMin}}$  and  $M_{\text{BHseed}}$ , we also vary the outflow velocity for BH kinetic feedback:  $v_w = (1000 - 10000) \text{ km/s}$ .

The earliest BHs appear at  $z \sim 18 - 25$  in our simulations, when the first halos reach the corresponding lower limit  $M_{\text{HaloMin}}$ . The BHs are allowed to grow by accreting surrounding gas and by merger with other BHs. As they accrete and grow, the BHs eject out feedback energy, and impact their host DGs. We find the following results for the growth and feedback of IMBHs in our simulations:

- The BHs grow to intermediate masses  $M_{\text{BH}} = \text{few} \times 10^5 - 10^6 M_{\odot}$  by  $z = 5$ , when the BHs are seeded in halos with  $M_{\text{HaloMin}} \leq 4 \times 10^7 M_{\odot}$ . The most-massive BH at  $z = 4$  has:  $M_{\text{BH}} = 2 \times 10^6 M_{\odot}$  and  $\dot{M}_{\text{BH}} = 0.02 M_{\odot}/\text{yr}$ .
- BHs seeded in smaller halos grow faster (considering the same redshift) than those seeded in larger halos. E.g. at  $z = 7$ , the most-massive BH in the simulation has grown to  $M_{\text{BH}} = 10^5 M_{\odot}$  when seeded in  $M_{\text{HaloMin}} = 2 \times 10^7 M_{\odot}$

halos, while it grows only to  $M_{\text{BH}} = 4 \times 10^4 M_{\odot}$  when seeded in  $M_{\text{HaloMin}} = 3 \times 10^7 M_{\odot}$  halos.

- The effect of increasing or decreasing the parameters  $M_{\text{HaloMin}}$  and  $M_{\text{BHseed}}$  together on the BH mass growth can be the same. E.g., a BH can grow similarly when seeded in smaller halos ( $M_{\text{HaloMin}} = 10^6 M_{\odot}$ ) with a smaller seed mass ( $M_{\text{BHseed}} = 10^2 M_{\odot}$ ), as in larger halos ( $M_{\text{HaloMin}} = 10^7 M_{\odot}$ ) with a higher seed mass ( $M_{\text{BHseed}} = 10^3 M_{\odot}$ ).

The variation in the BH outflow velocity has little effect upon the BH growth, although the increase of the outflow velocity delays the suppression of SF.

- Starting from highly sub-Eddington rates (Eddington ratio  $< 0.001$ ), the accretion rate of the BHs increases with time, and reaches  $\dot{M}_{\text{BH}} = (0.2 - 0.8)\dot{M}_{\text{Edd}}$  for the massive IMBHs by  $z = 4$ .

- Our simulations probe dwarf galaxies with a stellar mass between  $M_{\star} = (10^5 - 10^8)M_{\odot}$ . The star formation rate density evolution of these DGs has a wide maximum in the form of a plateau between  $z = 4 - 6$ , and the SFRD decreases at  $z > 6$  and at  $z < 4$ .

- Star-formation is quenched between  $z = 9 - 4$  by BH accretion and feedback. The SFRD is reduced by factors 1.1 – 3, when the BHs have grown to a mass  $M_{\text{BH}} \sim$  a few times  $10^5 M_{\odot}$ .

- There is a huge scatter in the BH - galaxy [ $M_{\text{BH}} - M_{\star}$ ] correlation of the simulated galaxies, especially at low- $M_{\star}$ .

In our runs where SF quenching happens the earliest, the IMBHs ( $M_{\text{BH}} = 10^3 - 10^5 M_{\odot}$ ) in DGs ( $M_{\star} = 10^4 - 10^7 M_{\odot}$ ) are already more massive at  $z = 7.9$ , as compared to the local [ $M_{\text{BH}} - M_{\star}$ ] correlation and that of high- $z$  quasars. Central BHs in some runs (*BHs3h3e7*, *BHs3h4e7*, *BHs3h5e7*) more or less follow the local  $z = 0$  correlation at  $z \geq 5.5$ .

- Varying the SN feedback strength (by a factor 2.5) has a little impact on the growth of the BHs. Our simulated BHs continue to grow up to  $z \sim 6$ , even in the presence of stronger SN-driven mass ejection, sustained by gas inflows driven by galaxy mergers and interactions in a cosmological environment.

- The IMBHs do not always show indications of BH feedback driven gas outflows. There are only signatures of outflows around the most-massive IMBHs with  $M_{\text{BH}} > 10^6 M_{\odot}$ , as shock-heated low-density gas.

- Our result of rapid BH growth at the centers of DGs suggest that these BHs grow faster than their host galaxies in the early Universe. The resulting early BH feedback quenches star formation, and possibly turns the dwarf galaxies (as well as their central BHs) dormant.

*We deduce that intermediate-mass black holes at the centers of dwarf galaxies can be a strong source of feedback. Our cosmological hydrodynamical simulations show that when the IMBHs have grown to  $10^5 M_{\odot}$ , they quench star formation in their host galaxies. At the same time, these IMBHs form the missing link between stellar-mass and supermassive BHs.*

## ACKNOWLEDGMENTS

We are most grateful to Volker Springel for allowing us to use the GADGET-3 code. This work is supported by the Brazilian Agencies FAPESP (grants 2016/01355-5, 2016/22183-8, and 2013/10559-5); and CNPq (grant 308643/2017-8).

## REFERENCES

- Afanasiev, A. V. et al. 2018, accepted in MNRAS, eprint arXiv:1804.02938
- Ahn, C. P. et al. 2018, eprint arXiv:1804.02399
- Angles-Alcazar, D., Faucher-Giguere, C.-A., Quataert, E., Hopkins, P. F., Feldmann, R., Torrey, P., Wetzell, A. & Keres, D. 2017, MNRAS, 472, L109
- Baldassare, V. F., Reines, A. E., Gallo, E. & Greene, J. E. 2015, ApJ, 809, L14
- Barai, P. 2008, ApJ, 682, L17
- Barai, P. et al. 2013, MNRAS, 430, 3213
- Barai, P., Viel, M., Murante, G., Gaspari, M. & Borgani, S. 2014, MNRAS, 437, 1456
- Barai, P., Monaco, P., Murante, G., Ragagnin, A. & Viel, M. 2015, MNRAS, 447, 266
- Barai, P., Murante, G., Borgani, S., Gaspari, M., Granato, G. L., Monaco, P. & Ragone-Figueroa, C. 2016, MNRAS, 461, 1548
- Barai, P., Gallerani, S., Pallottini, A., Ferrara, A., Marconi, A., Cicone, C., Maiolino, R. & Carniani, S. 2018, MNRAS, 473, 4003
- Bieri, R., Dubois, Y., Silk, J. & Mamon, G. A. 2015, ApJ, 812, L36
- Biffi, V., Borgani, S., Murante, G., Rasia, E., Planelles, S., Granato, G. L., Ragone-Figueroa, C., Beck, A. M., Gaspari, M. & Dolag, K. 2016, ApJ, 827, 112
- Bolton, C. T. 1972, Nature Physical Science, 240, 124
- Bondi, H. 1952, MNRAS, 112, 195
- Bouche, N., Hohensee, W., Vargas, R., Kacprzak, G. G., Martin, C. L., Cooke, J. & Churchill, C. W. 2012, MNRAS, 426, 801
- Bouwens, R. J. et al. 2009, ApJ, 705, 936
- Bouwens, R. J. et al. 2012, ApJ, 754, 83
- Caballero-Garcia, M. D., Fabrika, S., Castro-Tirado, A. J., Bursa, M., Dovciak, M., Castellon, A. & Karas, V. 2018, submitted to RMxAC, eprint arXiv:1802.07149
- Caproni, A., Amaral Lanfranchi, G., Campos Baio, G. H., Kowal, G., & Falceta-Goncalves, D. 2017, ApJ, 838, 99
- Chabrier, G. 2003, PASP, 115, 763
- Chambers, K. C., Miley, G. K. & van Breugel, W. 1987, Nature, 329, 604
- Chilingarian, I. V., Katkov, I. Y., Zolotukhin, I. Y., Grishin, K. A., Beletsky, Y., Boutsia, K. & Osip, D. J. 2018, submitted to ApJ, eprint arXiv:1805.01467
- Cicone, C. et al. 2014, A&A, 562, A21
- Corral-Santana, J. M., Casares, J., Munoz-Darias, T., Bauer, F. E., Martinez-Pais, I. G. & Russell, D. M. 2016, A&A, 587, A61
- Cowley, A. P., Crampton, D., Hutchings, J. B., Remillard, R. & Penfold, J. E. 1983, ApJ, 272, 118
- Crenshaw, D. M., Kraemer, S. B., & George, I. M. 2003, ARA&A, 41, 117
- Cucciati, O. et al. 2012, A&A, 539, A31
- Dashyan, G., Silk, J., Mamon, G. A., Dubois, Y. & Hartwig, T. 2018, MNRAS, 473, 5698
- Demers, S., Battinelli, P., Irwin, M. J. & Kunkel, W. E. 1995, MNRAS, 274, 491
- De Young, D. S. 1989, ApJ, 342, L59
- Di Matteo, T., Khandai, N., DeGraf, C., Feng, Y., Croft, R. A. C., Lopez, J. & Springel, V. 2012, ApJ, 745, L29
- Dubois, Y., Pichon, C., Devriendt, J., Silk, J., Haehnelt,

- M., Kimm, T. & Slyz, A. 2013, *MNRAS*, 428, 2885
- Dubois, Y., Volonteri, M., Silk, J., Devriendt, J., Slyz, A. & Teyssier, R. 2015, *MNRAS*, 452, 1502
- Fabian, A. C. 2012, *ARA&A*, 50, 455
- Ferland, G. J., Korista, K. T., Verner, D. A., Ferguson, J. W., Kingdon, J. B. & Verner, E. M. 1998, *PASP*, 110, 761
- Ferrarese, L., & Ford, H. 2005, *SSRv*, 116, 523
- Filippenko, A. V. & Sargent, W. L. W. 1989, *ApJ*, 342, L11
- Gebhardt, K. et al. 2000, *ApJ*, 539, L13
- Giesers, B. et al. 2018, *MNRAS*, 475, L15
- Goulding, A. D. & Alexander, D. M. 2009, *MNRAS*, 398, 1165
- Graham, A. W., Soria, R. & Davis, B. L. 2018, *MNRAS* accepted, eprint arXiv:1811.03232
- Haardt, F. & Madau, P. 2001, XXXVIth Rencontres de Moriond, XXIst Moriond Astrophysics Meeting, Editors D.M.Neumann & J.T.T.Van, 64
- Habouzit, M., Volonteri, M. & Dubois, Y. 2017, *MNRAS*, 468, 3935
- Hahn, O. & Abel, T. 2011, *MNRAS*, 415, 2101
- Hoyle, F. & Lyttleton, R. A. 1939, *Proc. Cam. Phil. Soc.*, 35, 405
- Izotov, Y. I. & Thuan, T. X. 2008, *ApJ*, 687, 133
- Johansson, P. H., Naab, T. & Burkert, A. 2009, *ApJ*, 690, 802
- Katz, N., Weinberg, D. H. & Hernquist, L. 1996, *ApJS*, 105, 19
- Kennicutt, R. C. 1998, *ApJ*, 498, 541
- Koudmani, S., Sijacki, D., Bourne, M. A. & Smith, M. C. 2019, *MNRAS*, 484, 2047
- Kovetz, E. D., Cholis, I., Kamionkowski, M. & Silk, J. 2018, eprint arXiv:1803.00568
- Kraemer, S. B., Tombesi, F. & Bottorff, M. C. 2018, *ApJ*, 852, 35
- Kunth, D., Sargent, W. L. W. & Bothun, G. D. 1987, *AJ*, 93, 29
- Lanz, L., Ogle, P. M., Alatalo, K. & Appleton, P. N. 2016, *ApJ*, 826, 29
- Lemons, S. M., Reines, A. E., Plotkin, R. M., Gallo, E. & Greene, J. E. 2015, *ApJ*, 805, 12
- Maccarone, T. J., Kundu, A., Zepf, S. E. & Rhode, K. L. 2007, *Natur*, 445, 183
- Magorrian, J. et al. 1998, *AJ*, 115, 2285
- Marconi, A. & Hunt, L. K. 2003, *ApJ*, 589, L21
- Marleau, F. R., Clancy, D., Habas, R. & Bianconi, M. 2017, *A&A*, 602, A28
- Martin, C. L. 1999, *ApJ*, 513, 156
- Martin-Navarro, I. & Mezcua, M. 2018, *ApJ*, 855, L20
- McConnell, N. J. & Ma, C.-P. 2013, *ApJ*, 764, 184
- Melioli, C., de Gouveia Dal Pino, E. M. & Geraissate, F. G. 2013, *MNRAS*, 430, 3235
- Melioli, C. & de Gouveia Dal Pino, E. M. 2015, *ApJ*, 812, 90
- Mezcua, M., Civano, F., Marchesi, S., Suh, H., Fabbiano, G. & Volonteri, M. 2018a, *MNRAS*, 478, 2576
- Mezcua, M., Kim, M., Ho, L. C. & Lonsdale, C. J. 2018b, *MNRAS*, 480, L74
- Miller, J. M., Fabbiano, G., Miller, M. C. & Fabian, A. C. 2003, *ApJ*, 585, L37
- Moran, E. C., Shahinyan, K., Sugarman, H. R., Velez, D. O. & Eracleous, M. 2014, *AJ*, 148, 136
- Mortlock, D. J. et al. 2011, *Nature*, 474, 616
- Mukherjee, D., Bicknell, G. V., Wagner, A. Y., Sutherland, R. S. & Silk, J. 2018, *MNRAS*, 479, 5544
- Orosz, J. A. et al. 2007, *Nature*, 449, 872
- Penny, S. J. et al. 2017, submitted to *MNRAS*, eprint arXiv:1710.07568
- Perez-Gonzalez, P. G. et al. 2005, *ApJ*, 630, 82
- Peterson, B. M. et al. 2005, *ApJ*, 632, 799
- Planck Collaboration; Ade, P. A. R. et al. 2016, *A&A*, 594, A13
- Prieto, J., Escala, A., Volonteri, M. & Dubois, Y. 2017, *ApJ*, 836, 216
- Reddy, N. A. & Steidel, C. C. 2009, *ApJ*, 692, 778
- Rees, M. J. 1984, *ARA&A*, 22, 471
- Reines, A. E., Sivakoff, G. R., Johnson, K. E. & Brogan, C. L. 2011, *Nature*, 470, 66
- Reines, A. E., Greene, J. E. & Geha, M. 2013, *ApJ*, 775, 116
- Reines, A. E. & Volonteri, M. 2015, *ApJ*, 813, 82
- Rodighiero, G. et al. 2010, *A&A*, 515, A8
- Salmon, B. et al. 2015, *ApJ*, 799, 183
- Salome, Q., Salome, P., Miville-Deschenes, M.-A., Combes, F. & Hamer, S. 2017, *A&A*, 608, A98
- Santini, P. et al. 2017, *ApJ*, 847, 76
- Scannapieco, E., Silk, J. & Bouwens, R. 2005, *ApJ*, 635, L13
- Schawinski, K. et al. 2006, *Nature*, 442, 888
- Schaye, J. et al. 2015, *MNRAS*, 446, 521
- Schiminovich, D. et al. 2005, *ApJ*, 619, L47
- Schmidt, M. 1959, *ApJ*, 129, 243
- Schramm, M. et al. 2013, *ApJ*, 773, 150
- Secretst, N. J. et al. 2015, *ApJ*, 798, 38
- Seth, A. C. et al. 2010, *ApJ*, 714, 713
- Shakura, N. I. & Sunyaev, R. A. 1973, *A&A*, 24, 337
- Sijacki, D., Springel, V., Di Matteo, T. & Hernquist, L. 2007, *MNRAS*, 380, 877
- Silk, J., & Rees, M. J. 1998, *A&A*, 331, L1
- Silk, J. 2017, *ApJ*, 839, L13
- Springel, V. & Hernquist, L. 2003, *MNRAS*, 339, 289
- Springel, V. 2005, *MNRAS*, 364, 1105
- Springel, V., Di Matteo, T. & Hernquist, L. 2005, *MNRAS*, 361, 776
- Sutton, A. D., Roberts, T. P., Walton, D. J., Gladstone, J. C. & Scott, A. E. 2012, *MNRAS*, 423, 1154
- Tescari, E., Viel, M., D'Odorico, V., Cristiani, S., Calura, F., Borgani, S. & Tornatore, L. 2011, *MNRAS*, 411, 826
- Thornton, C. E., Barth, A. J., Ho, L. C., Rutledge, R. E. & Greene, J. E. 2008, *ApJ*, 686, 892
- Tombesi, F., Melendez, M., Veilleux, S., Reeves, J. N., Gonzalez-Alfonso, E. & Reynolds, C. S. 2015, *Nature*, 519, 436
- Tornatore, L., Borgani, S., Dolag, K. & Matteucci, F. 2007, *MNRAS*, 382, 1050
- Trebitsch, M., Volonteri, M., Dubois, Y. & Madau, P. 2018, *MNRAS*, 478, 5607
- Tremmel, M., Governato, F., Volonteri, M. & Quinn, T. R. 2015, *MNRAS*, 451, 1868
- Urry, C. M. & Padovani, P. 1995, *PASP*, 107, 803
- Valluri, M., Ferrarese, L., Merritt, D. & Joseph, C. L. 2005, *ApJ*, 628, 137
- van der Burg, R. F. J., Hildebrandt, H. & Erben, T. 2010, *A&A*, 523, A74

- van der Marel, R. P., Cretton, N., de Zeeuw, P. T. & Rix, H.-W. 1998, *ApJ*, 493, 613
- van der Marel, R. P. 2004, *Carnegie Observatories Astrophysics Series*. eds Ho, L. C. CUP, 37
- Viegas, S. M. & de Gouveia dal Pino, E. M. 1992, *ApJ*, 384, 467
- Volonteri, M. & Natarajan, P. 2009, *MNRAS*, 400, 1911
- Wang, R. et al. 2010, *ApJ*, 714, 699
- Wiersma, R. P. C., Schaye, J. & Smith, B. D. 2009, *MNRAS*, 393, 99
- Woo, J.-H., Cho, H., Gallo, E., Hodges-Kluck, E., Le, H. A., Shin, J., Son, D. & Horst, J. C. 2019, eprint arXiv:1905.00145, in press
- Wurster, J. & Thacker, R. J. 2013, *MNRAS*, 431, 2513
- Zinn, P.-C., Middelberg, E., Norris, R. P. & Dettmar, R.-J. 2013, *ApJ*, 774, 66